

This is a self-archived version of an original article. This version may differ from the original in pagination and typographic details.

Author(s): Wasiljeff, Joonas; Salminen, Johanna M.; Roberts, Andrew P.; Hu, Pengxiang; Brown, Maxwell; Kuva, Jukka; Lukkari, Sari; Jolis, Ester M.; Heinsalu, Atko; Hong, Wei-Li; Lepland, Aivo; Suuroja, Sten; Parkkonen, Joni; Virtasalo, Joonas J.

Title: Morphology-Dependent Magnetic Properties in Shallow-Water Ferromanganese Concretions

Year: 2024

Version: Published version

Copyright: © 2024 The Author(s). Geochemistry, Geophysics, Geosystems published by Wiley

Rights: CC BY 4.0

Rights url: <https://creativecommons.org/licenses/by/4.0/>

Please cite the original version:

Wasiljeff, J., Salminen, J. M., Roberts, A. P., Hu, P., Brown, M., Kuva, J., Lukkari, S., Jolis, E. M., Heinsalu, A., Hong, W., Lepland, A., Suuroja, S., Parkkonen, J., & Virtasalo, J. J. (2024). Morphology-Dependent Magnetic Properties in Shallow-Water Ferromanganese Concretions. *Geochemistry, Geophysics, Geosystems*, 25(5), Article e2023GC011366. <https://doi.org/10.1029/2023gc011366>

Geochemistry, Geophysics, Geosystems®








RESEARCH ARTICLE

10.1029/2023GC011366

Morphology-Dependent Magnetic Properties in Shallow-Water Ferromanganese Concretions

Key Points:

- Magnetic minerals within shallow water Fe-Mn concretions can provide valuable environmental information about their formation
- Magnetic properties are linked to specific growth patterns in Baltic Sea Fe-Mn concretions
- Spheroidal and crust/discoidal concretions are dominated by biogenic and pedogenic magnetic phases, respectively

Joonas Wasiljeff¹ , Johanna M. Salminen^{1,2}, Andrew P. Roberts³ , Pengxiang Hu³, Maxwell Brown⁴, Jukka Kuva¹, Sari Lukkari¹, Ester M. Jolis¹, Atko Heinsalu⁵ , Wei-Li Hong^{6,7} , Aivo Lepland^{5,8}, Sten Suuroja⁹, Joni Parkkonen¹⁰, and Joonas J. Virtasalo¹ 

¹Geological Survey of Finland (GTK), Espoo, Finland, ²Department of Geosciences and Geography, University of Helsinki, Helsinki, Finland, ³Research School of Earth Sciences, Australian National University, Canberra, ACT, Australia, ⁴Department of Earth and Environmental Sciences, Institute for Rock Magnetism, University of Minnesota, Minneapolis, MN, USA, ⁵Department of Geology, Tallinn University of Technology, Tallinn, Estonia, ⁶Department of Geological Sciences, Stockholm University, Stockholm, Sweden, ⁷Baltic Sea Centre, Stockholm University, Stockholm, Sweden, ⁸Geological Survey of Norway, Trondheim, Norway, ⁹Geological Survey of Estonia, Rakvere, Estonia, ¹⁰Department of Physics and Nanoscience Center, University of Jyväskylä, Jyväskylä, Finland

Supporting Information:

Supporting Information may be found in the online version of this article.

Correspondence to:

J. Wasiljeff,
joonas.wasiljeff@gtk.fi

Citation:

Wasiljeff, J., Salminen, J. M., Roberts, A. P., Hu, P., Brown, M., Kuva, J., et al. (2024). Morphology-dependent magnetic properties in shallow-water ferromanganese concretions. *Geochemistry, Geophysics, Geosystems*, 25, e2023GC011366. <https://doi.org/10.1029/2023GC011366>

Received 21 NOV 2023

Accepted 6 MAY 2024

Abstract Ferromanganese concretions commonly occur in shallow-water coastal regions worldwide. In the Baltic Sea, they can record information about past and present underwater environments and could be a potential source for critical raw materials. We report on their microstructural characteristics and magnetic properties and link them to their formation mechanisms and environmental significance. Microstructural investigations from nano- and micro-computed tomography, electron microscopy, and micro-X-ray fluorescence elemental mapping reveal diverse growth patterns within concretions of different morphologies. Alternating Fe- and Mn-rich growth bands indicate fluctuating redox conditions during formation. Bullet-shaped magnetofossils, produced by magnetotactic bacteria, are present, which suggests the influence of bacterial activity on concretion formation. Spheroidal concretions, which occur in deeper and more tranquil environments, have enhanced microbial biomineralization and magnetofossil preservation. Conversely, crusts and discoidal concretions from shallower and more energetic environments contain fewer magnetofossils and have a greater detrital content. Our results provide insights into concretion formation mechanisms and highlight the importance of diagenetic processes, oxygen availability, and bacterial activity in the Baltic Sea.

1. Introduction

Ferromanganese (Fe-Mn) concretions are distributed widely, extending beyond deep ocean environments to encompass the shelf seas of the world, with notable occurrences in the north-eastern Atlantic Ocean, South China Sea, Kara Sea, Black Sea, Barents Sea, and Baltic Sea (Baturin, 2010; González et al., 2010; Vereshchagin et al., 2019; Zhamoida et al., 2017; Zhong et al., 2017). In the Baltic Sea, early reports of Fe-Mn concretions were made in the late 19th and early 20th centuries (e.g., Grewingk, 1884; Hesse, 1924), but the first major studies of these precipitates were not carried out until the 1960s and 1970s (e.g., Glasby et al., 1997; Winterhalter & Siivola, 1967). Recently, Fe-Mn concretions have gained increased economic and scientific attention globally due to their importance as underwater habitats, as sources of critical metals, and due to their ability to record paleoceanographic and paleoenvironmental changes (e.g., Hannington et al., 2017; Hein et al., 2020; Jiang et al., 2022; Kaikkonen et al., 2019).

Authigenic Fe-Mn concretion formation is typically confined to the seafloor in areas experiencing low or no net sediment deposition and organic matter loading with colloidal iron and manganese oxyhydroxides supplied from the surrounding catchment area and/or from adjacent anoxic marine sediments due to diagenetic remobilization (Ingri & Pontér, 1986; Marcus et al., 2004; Zhamoida et al., 2007). Their formation is redox driven and often creates concretions with alternating Fe and Mn layers reflecting redox fluctuations (Axelsson et al., 2002; Gasparatos et al., 2005; Winterhalter & Siivola, 1967). Fe and Mn (oxyhydr)oxides effectively scavenge trace elements, including cobalt and rare earth elements (REEs), from seawater, which attests to their economic importance. Typically, the Fe and Mn phases are poorly crystalline or X-ray amorphous Fe and Mn hydroxides, but 2-line ferrihydrite and turbostratic birnessite have also been observed (Marcus et al., 2004). In the Baltic Sea, concretions are porous and have various sizes and shapes (i.e., crust, discoidal, and spheroidal) and harbor diverse microbial communities with reductive and oxidative metabolisms that can influence both concretion growth and

© 2024 The Author(s). Geochemistry, Geophysics, Geosystems published by Wiley Periodicals LLC on behalf of American Geophysical Union. This is an open access article under the terms of the [Creative Commons Attribution License](https://creativecommons.org/licenses/by/4.0/), which permits use, distribution and reproduction in any medium, provided the original work is properly cited.

dissolution (Yli-Hemminki et al., 2014; Zhang et al., 2002). These brackish water concretions grow exceptionally rapidly, averaging tens of μm per year (Grigoriev et al., 2013; Liebetrau et al., 2002) compared to typical growth rates of a few mm per Myr on the deep ocean floor (e.g., Frank et al., 1999; Klemm et al., 2005; Marcus et al., 2015). This suggests microbial catalysis in their growth that enables them to record recent environmental processes at high-resolution over thousands of years timescales.

Fe-Mn concretions cover ca. 10% of the Baltic seafloor at 20–100 m water depths (Glasby et al., 1997; Kaikkonen et al., 2019). Generally, the concretion-bearing seafloor surface is covered by a thin (10–20 mm thick) layer of fluffy, organic-rich mud (Zhamoïda et al., 2017), with concretions exposed on the seafloor in some areas. Fe-Mn concretions most frequently occur along the peripheries of major seafloor depressions (Glasby et al., 1997). Conversely, shallower areas at depths of less than 40 m contain only sporadic concretion occurrences (Zhamoïda et al., 2007). Concretion fields are notably prevalent in regions where Precambrian Baltic Shield crystalline rocks compose the underlying strata due to their high Mn and Fe contents. The prevailing hypothesis posits that glacial till, originating from these rocks, is the primary Mn and Fe source for concretion formation (Callender & Bowser, 1976). Also, glaciolacustrine rhythmites and post-glacial lacustrine clays, which cover the crystalline bedrock and till, have elevated reactive Mn and Fe contents (Virtasalo & Kotilainen, 2008). Concretion abundance and Mn content generally increase with increasing water depth due to greater Mn mobilization and migration in anoxic environments of the deepest basins (Force & Cannon, 1988; Huckriede & Meischner, 1996; Lenz et al., 2015).

River discharge is a further important source of Fe and Mn in the Baltic Sea (Winterhalter, 1980; Zhamoïda et al., 1996). In the easternmost Baltic Sea (the Gulf of Finland), where abundant spheroidal, discoidal, and crust concretions occur, the Neva River plume carries Fe and Mn to the gulf. In the northernmost Baltic Sea (the Gulf of Bothnia), into which the Kokemäenjoki River and several smaller rivers discharge, concretions are most abundant in Bothnian Bay (Glasby et al., 1997). This area is characterized by Fe-rich crust concretions, although spheroidal morphotypes are also frequently encountered. In the southwestern tip of Finland, at the confluence of the two gulfs, the Archipelago Sea receives river discharge from two of the largest rivers in the region, the Aurajoki and Paimionjoki rivers. In this area, all the three morphotypes are common.

It is well-established that Fe-Mn concretions can have stable magnetism and that slow-growing deep ocean Fe-Mn crusts and nodules can record multiple geomagnetic field reversals over millions of years (e.g., Chan et al., 1985; Crecelius et al., 1973; Oda et al., 2011). However, the magnetic properties of ferrimagnetic minerals in concretions and the origin of their natural remanent magnetization are only starting to be understood. Recent discoveries have shown that biogenic magnetite contributes to a biogeochemical remanent magnetization in deep ocean crusts and nodules (Hassan et al., 2020; Jiang et al., 2020; Oda et al., 2018; Yuan et al., 2020), which indicates the impact of abyssal microbial communities on nodule biomineralization. While extensive studies on the magnetic properties and magnetostratigraphic dating of deep ocean concretions have been carried out (e.g., Jiang et al., 2021; Joshima & Usui, 1998; Oda et al., 2023), no such investigations have been undertaken on fast-growing shallow water concretions in shelf seas such as the Baltic Sea. Furthermore, the specific mechanisms of concretion formation and (bio)mineralization for different Baltic Sea morphotypes remain poorly understood. In this study, we investigate the origin of remanent magnetization in Baltic Sea Fe-Mn concretions and compare how their internal structure and morphotype influence their magnetic properties.

2. Material and Methods

2.1. Study Area and Sample Preparation

In 2021 and 2022, research cruises by the RV *Geomari* and RV *Electra* targeted the eastern and western parts of the Gulf of Finland, the Archipelago Sea, and the Gulf of Bothnia (Figure 1). Abundant Fe-Mn concretions of various sizes and morphotypes were collected, with crust, discoidal, and spheroidal morphotypes selected for analysis (Figure 2; Table 1, sample code prefixes MGBC and 22GoF). Further samples were provided by the Tallinn University of Technology (sample code SLM, Table 1). Of these samples, two Fe-Mn concretions with characteristics of all three morphotypes were selected for detailed microstructural, geochemical, and magnetic analysis. Sample MGBC-2021-4-1 is a Fe-rich crust-like concretion with discoidal growth bands around a nucleus that extend approximately horizontally along the sediment-water interface, and sample 22GoF-16-1 is a Mn-rich spheroidal concretion with ca. 4 cm diameter. Both samples were flushed with ultrapure water and frozen with dry ice immediately after collection with a box corer. The frozen samples were then freeze-dried at the

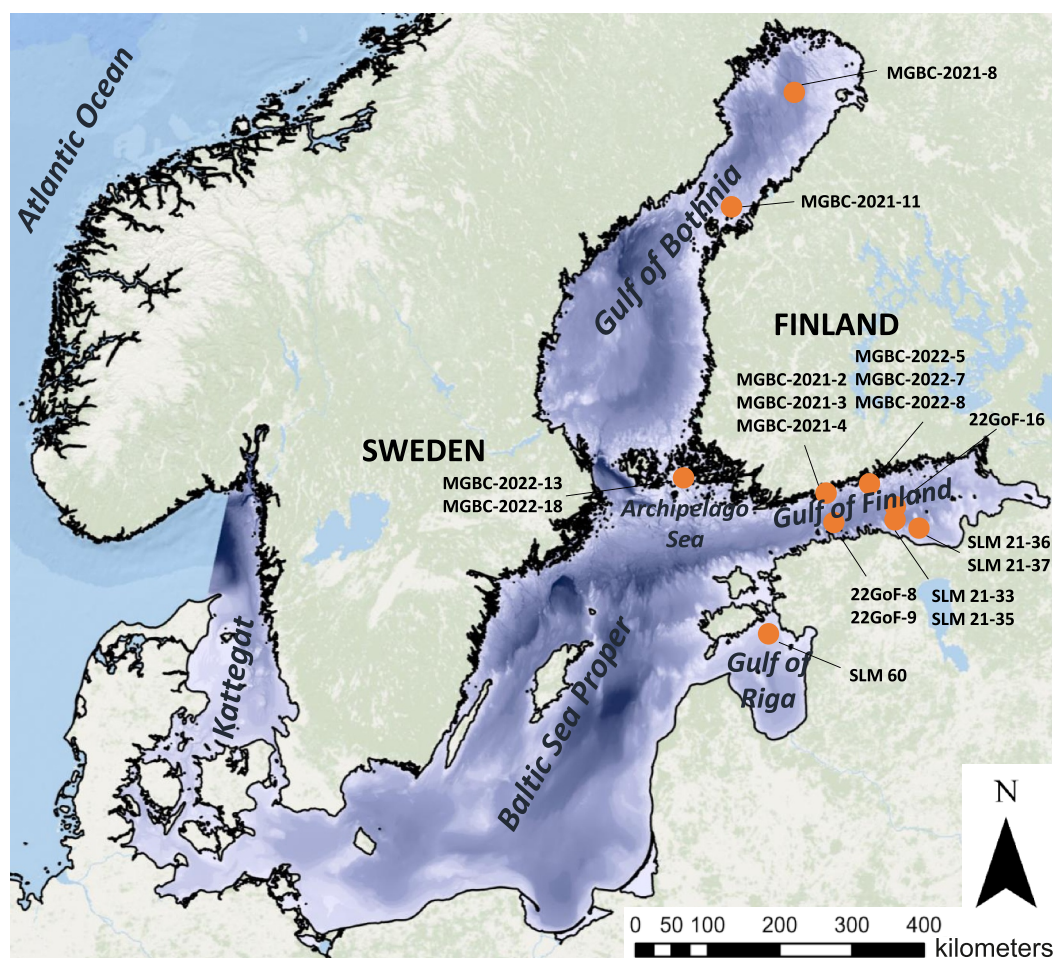


Figure 1. Map of Fe-Mn concretion sample locations (orange circles) in the Baltic Sea region. Bathymetry is presented only for the Baltic Sea basin. Base map: ESRI Inc. (Redlands) Ocean Basemap 2018. Bathymetric data: EMODnet Bathymetry 2018 (Thierry et al., 2019).

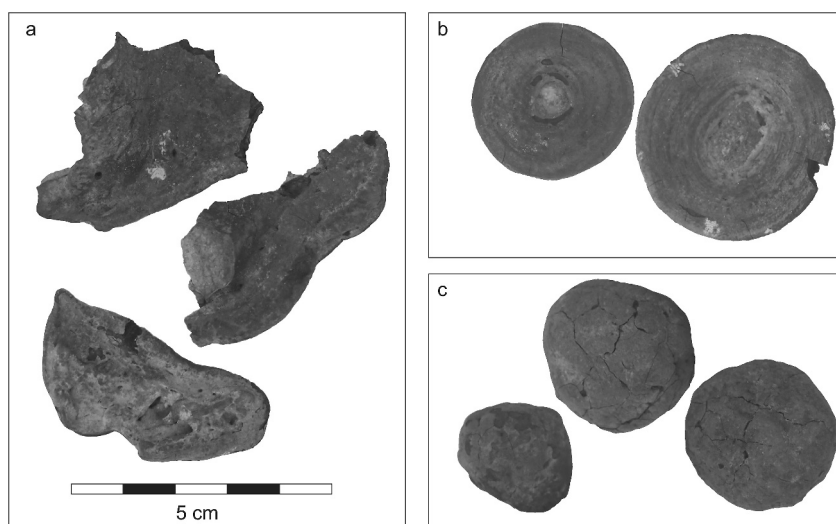


Figure 2. End member morphotypes of Baltic Sea Fe-Mn concretions. (a) Crust, (b) discoidal, and (c) spheroidal. All images have the same scale. Irregular concretions and unique combinations of the three types are also common.

Table 1
List of Studied Fe-Mn Concretion Samples From the Baltic Sea

Sample name	Morphotype	Location	Latitude (N)	Longitude (E)	Water depth (m)
MGBC-2021-2-S-T1	Spheroidal	GoF	59°57.591	24°46.101	57.2
MGBC-2021-2-S-T2	Spheroidal	GoF	59°57.591	24°46.101	57.2
MGBC-2021-2-S-T3	Spheroidal	GoF	59°57.591	24°46.101	57.2
MGBC-2021-2-S-T4	Spheroidal	GoF	59°57.591	24°46.101	57.2
MGBC-2021-3-S-T1	Spheroidal	GoF	59°57.846	24°46.440	50.9
MGBC-2021-3-S-T2	Spheroidal	GoF	59°57.846	24°46.440	50.9
MGBC-2021-3-S-T3	Spheroidal	GoF	59°57.846	24°46.440	50.9
MGBC-2021-8-S-T1	Spheroidal	GoB	64°52.027	23°14.624	73.0
MGBC-2021-8-S-T2	Spheroidal	GoB	64°52.027	23°14.624	73.0
MGBC-2021-8-S-T3	Spheroidal	GoB	64°52.027	23°14.624	73.0
MGBC-2021-8-S-T4	Spheroidal	GoB	64°52.027	23°14.624	73.0
MGBC-2021-8-S-T5	Spheroidal	GoB	64°52.027	23°14.624	73.0
MGBC-2021-8-S-T6	Spheroidal	GoB	64°52.027	23°14.624	73.0
MGBC-2022-8-D/S-T1	Spheroidal	GoF	60°01.000	26°04.812	60.0
SLM 21-33-S-T1	Spheroidal	GoF	59°40.470	26°33.120	30.8
MGBC-2022-7-S-T1	Spheroidal	GoF	60°05.493	25°57.789	44.0
MGBC-2022-7-S-T2	Spheroidal	GoF	60°05.493	25°57.789	44.0
MGBC-2022-7-4	Spheroidal	GoF	60°05.493	25°57.789	44.0
MGBC-2022-7-fluffy	<i>Organic-rich mud</i>	GoF	60°05.493	25°57.789	44.0
22GoF-8_LAB1	Spheroidal	GoF	59°43.510	24°53.570	95.0
22GoF-9_LAB1	Spheroidal	GoF	59°43.534	24°53.662	95.0
22GoF-16-1	Spheroidal	GoF	59°55.110	26°20.537	80.0
MGBC-2021-4-1	Crust	GoF	59°57.929	24°46.726	45.4
MGBC-2021-4-C-T1	Crust	GoF	59°57.929	24°46.726	45.4
MGBC-2021-4-C-T2	Crust	GoF	59°57.929	24°46.726	45.4
MGBC-2021-4-C-T3	Crust	GoF	59°57.929	24°46.726	45.4
MGBC-2021-11-C-T1	Crust	GoB	63°33.747	21°54.616	32.2
MGBC-2021-11-C-T2	Crust	GoB	63°33.747	21°54.616	32.2
MGBC-2021-11-C-T3	Crust	GoB	63°33.747	21°54.616	32.2
MGBC-2022-13-C-T1	Crust	AS	60°05.569	21°16.312	51.0
MGBC-2022-13-C-T2	Crust	AS	60°05.569	21°16.312	51.0
SLM 60-D-T1	Discoidal	GoR	58°9.670	23°30.369	27.0
SLM 21-35-D-T1	Discoidal	GoF	59°38.673	26°43.073	36.2
SLM 21-37-D-T1	Discoidal	GoF	59°33.000	26°52.272	30.8
SLM 21-36-D-T1	Discoidal	GoF	59°33.034	26°52.259	31.2
MGBC-2022-5-D-1	Discoidal	GoF	60°11.483	26°01.895	29.0
MGBC-2022-18-D-T1	Discoidal	AS	60°02.746	21°35.102	18.0

Note. Abbreviations for locations in the Baltic Sea: AS = Archipelago Sea, GoB = Gulf of Bothnia, GoF = Gulf of Finland, GoR = Gulf of Riga. Samples with the prefix SLM are provided by the Tallinn University of Technology, Estonia.

Geological Survey of Finland (GTK), Espoo, Finland. After drying, the samples became fragile and were impregnated with epoxy resin (Struers EpoFix). The resin-embedded concretions were then cut in half. One other half was prepared into an epoxy button or thin section for electron microscope imaging and micro-X-ray fluorescence (μ XRF) analyses at the GTK and the other half was cut into slices perpendicular to growth layers with a

precision saw for magnetic measurements. MGBC-2021-4-1 was cut into 25 pieces (Figure S1 in Supporting Information S1); specimens 13 to 25 were subjected to rock magnetic measurements. In contrast, sample 22GoF-16-1 was sliced into seven specimens for magnetic property investigations (Figure S2 in Supporting Information S1).

2.2. Magnetic Methods

Bulk magnetic measurements were made at the Solid Earth Geophysics Laboratory, University of Helsinki, Finland, and at the Geophysical Laboratory, GTK. Low-frequency susceptibility (χ_{lf}) was measured in a 200 A/m field at 976 Hz and high-frequency susceptibility (χ_{hf}) at 15,616 Hz with an AGICO MFK-1A Kappabridge. Frequency dependent magnetic susceptibility (χ_{fd}) was calculated as $\chi_{fd} = \chi_{hf} - \chi_{lf}$. An anhysteretic remanent magnetization (ARM) was imparted using a peak field of 100 mT and a direct current bias field of 50 μ T with an AGICO LDA-3A. An isothermal remanent magnetization (IRM) up to 3 T was imparted with a Magnetic Measurements MMPM10 Pulse Magnetizer. ARMs and IRMs were demagnetized with alternating fields (AF) and remanences were measured with a 2G Enterprises superconducting rock magnetometer. Magnetic grain-size (χ_{ARM}/χ_{lf} , χ_{ARM}/χ_{fd} , χ_{ARM}/IRM_{100}), bulk concentration (χ_{lf}/IRM_{100}), and coercivity ($HIRM_{AF100}$) dependent parameters were calculated. χ_{ARM}/χ_{lf} and χ_{ARM}/IRM_{100} can be used as proxies for biogenic magnetite (Egli, 2004a; Oldfield, 2013; Zhang et al., 2022). IRM_{100} is equivalent to IRM acquisition at 100 mT. The ratio of the “hard” IRM ($HIRM$) after AF demagnetization at 100 mT to SIRM at 3 T [$(IRM_{AF100\text{ mT}}/SIRM_{3T}) \times 100\%$] was calculated as $HIRM_{AF100}$ to reflect the relative contribution from magnetic minerals with coercivity of remanence (B_{cr}) larger than 100 mT.

High temperature (T) thermomagnetic analyses (χ vs. T) of selected powdered concretion samples were made with an AGICO KLY-3S-CS3 Kappabridge system. The samples were heated from room temperature to 700°C and cooled back to room temperature in argon, while the bulk susceptibility was measured continuously. The Cureval 8.0.2. software (<http://www.agico.com>) was used to determine Curie temperatures.

Room temperature hysteresis loops and first-order reversal curve (FORC) measurements were made at the Australian National University (ANU), Canberra, Australia, with a Princeton Measurements Corporation MicroMag 3900 vibrating sample magnetometer (VSM), and at the Institute for Rock Magnetism, University of Minnesota, Minneapolis, USA, using a LakeShore 8600 series VSM. In addition to obtaining conventional FORC diagrams (Pike et al., 1999; Roberts et al., 2000), which represent a convolution of remanent, induced, and transient magnetization (Hu et al., 2018; Roberts et al., 2019; Zhao et al., 2017), the protocol of Zhao et al. (2017) was followed to produce remanence (remFORC), induced (iFORC), and transient (tFORC) diagrams, respectively.

Selected samples were processed with the xFORC 4.0 software (Zhao et al., 2015) to obtain additional information for domain state diagnosis: hysteresis loops were measured between ± 300 mT or ± 500 mT in 2.5 mT steps and were used to generate irregular grids for the different FORC-type measurements with the xFORC software. An averaging time of 300 ms was used and data were processed with SF = 3 for all measurements. Detailed magnetic measurements were made on sub-samples of the two cut samples (22GoF-16-1 and MGBC-2021-4-1) at the Institute for Rock Magnetism. Hysteresis loops were measured to ± 500 mT in 1 mT steps, with a 300 ms averaging time at each step. Direct current demagnetization (DCD) curves were measured after applying a +2.5 T saturation isothermal magnetization (SIRM) with 150 backfield steps increasing to -2.5 T. A 700 μ T step size was used to measure 372 FORCs to 1.5 T (1.5 ms averaging time) or for 220 FORCs at a 2 mT step size to 1.5 T (300 ms averaging time). FORCs were processed in the FORCinel software (Harrison & Feinberg, 2008) employing the VARIFORC algorithm of Egli (2013). Coercivity spectra were assessed by converting DCD curves into IRM acquisition curves and unmixing their first derivatives into cumulative log Gaussian functions with the MAX UnMix software (Maxbauer et al., 2016).

Low-temperature remanence and susceptibility measurements were made with a Quantum Design Magnetic Property Measurement System (MPMS-3) at the Institute for Rock Magnetism, and with an MPMS XL-7 at ANU. Remanence was measured on warming from 10 to 300 K in zero field after cooling from 300 to 10 K either in a 2.5 T (or 5 T at ANU) field (FC) or in zero field cooling (ZFC) with a 2.5 T (or 5 T) field imparted at 10 K then set to zero prior to measurement. Following this, low temperature cycling of a room-temperature (300 K) saturation isothermal remanent magnetization (RT-SIRM) was measured, where a 2.5 T (or 5 T) SIRM was imparted at 300 K, after which remanence was measured while cooling from 300 to 10 K and warming to 300 K in zero field.

Temperature and frequency dependence of in-phase (χ') and out-of-phase (χ'') AC magnetic susceptibility were measured with an MPMS-3 from 10 to 300 K at 5 K intervals in a 239 A/m applied field at frequencies of 1 Hz, 10 Hz, and 100 Hz. Additionally, low-temperature hysteresis loops for selected samples were measured at 25 K, 35 and 50 K with the MPMS-3.

2.3. Microscopic and Microspectroscopic Methods

Nano-computed tomography (Nano-CT) was undertaken at the Nanoscience Center of the University of Jyväskylä, Finland, using Xradia NanoXCT-100 tomographic device. An X-ray energy of 8 keV was applied during imaging with a field of view of $65 \mu\text{m} \times 65 \mu\text{m}$, and image pixel size of 65 nm. A total of 1,081 projection images were taken over 180° of rotation. A 220 s exposure time was used for each projection, resulting in a total scanning time of 66 hr. The shadowgrams were registered after the scan using a tiny gold particle that was attached to the sample before imaging. Registration—that is, setting a fixed point in every image—is needed for reconstruction because the motion error of the sample stage is higher than the image resolution. Finally, a cylindrical CT volume with 60- μm diameter and 60- μm height and 65-nm voxel size was obtained using the Xradia TXMreconstructor software.

Micro-computed tomography (μCT) was undertaken using a GE phoenix v|tomelxs at the GTK Research laboratory, Espoo. All samples were scanned with a 240 kV microfocus tube with varying accelerating voltages of 100–200 kV, tube currents between 69 and 1,250 μA , and resulting powers between 8.6 and 200 W. Beam filters were 1.0 mm, 0.5 mm, or 0.1 mm of copper. No beam filters were used for some scans. 1,600–5,400 projections were taken from each sample, with the detector always waiting for a single exposure time and then taking an average over three exposures. Single exposure times ranged between 131 and 1,000 ms for a total scan time between 16 and 360 min and a spatial resolution between 8.6 and 121.9 μm . No ring artifact reduction was used in the reconstruction and the beam hardening correction coefficient (0–10) was 0, 4, or 8.

Micro X-Ray fluorescence (μXRF) imaging of Fe-Mn concretions was performed on a Bruker M4 Tornado AMICS μXRF scanner, which uses a 30 W Rh anode X-ray tube and two 30 mm^2 silicon drift detectors (SDDs) with <145 eV resolution ($\text{MnK}\alpha$) at 275 kcps. The Rh source was operated under maximum energy settings of 50 kV and 600 μA . The beam was focused with a polycapillary lens on a fixed 20 μm spot size under 2 mbar vacuum. The samples were mapped in separate runs with a 10–12 μm step size and 10 ms pixel dwell time. Qualitative elemental maps were generated with the Bruker M4 software.

Scanning electron microscope (SEM) imaging was carried out with a JEOL JSM-7100F Schottky Field Emission Scanning Electron Microscope (FE-SEM) equipped with an Oxford Instruments EDS-spectrometer X-Max 80 mm^2 (SDD) at 20 kV acceleration voltage and a 1.3 nA probe current. Both SEM imaging and SEM-based energy dispersive X-ray spectroscopy (EDS) analyses were undertaken in the backscattered electron (BSE) mode. BSE maps reveal compositional differences and EDX elemental maps display characteristic X-ray intensities of elements in the concretions. The maps were generated with Aztec software.

For transmission electron microscope (TEM) observations, particles were extracted by suspending ca. 1 g of powdered concretion material in 100 ml of MilliQ water in a beaker (250 ml) and then sonicating the suspension. Particles were then extracted with an Nd bar magnet covered with a Teflon tube following Li et al. (2012). Cleansing steps were repeated several times after which magnetic particles were deposited on a carbon coated Cu TEM grid. Extracted crystals were imaged with a JEOL 2100F TEM operating at 200 kV at the Center for Advanced Microscopy (CAM), ANU, Canberra, Australia. TEM images were acquired in bright field mode while EDS elemental maps were acquired with a scanning transmission electron microscope (STEM) using the High Angular Annular Dark Field (HAADF) mode.

3. Results and Discussion

3.1. Magnetic Characteristics of Baltic Sea Fe-Mn Concretions

Bulk concentration-dependent magnetic properties (χ_{lf} , χ_{ARM} , IRM_{100} , and SIRM) of investigated Fe-Mn concretions indicate that spheroidal morphotypes generally have higher values than the other two morphotypes (Table 2). Assuming that these parameters reflect the total ferrimagnetic mineral concentration, the abundance of these minerals in Baltic Sea concretions is similar or slightly greater than in some deep Pacific Ocean hydro-genetic nodules (cf. Jiang et al., 2020, 2022; Oda et al., 2023), but the single-domain (SD) magnetite content is

Table 2
Magnetic Properties of Baltic Sea Fe-Mn Concretions

Sample name	χ_{lf} (10^{-8} m ³ kg ⁻¹)	χ_{fd} (10^{-8} m ³ kg ⁻¹)	χ_{ARM} (10^{-8} m ³ kg ⁻¹)	IRM ₁₀₀ (10^{-5} Am ² kg ⁻¹)	SIRM (10^{-5} Am ² kg ⁻¹)	HIRM _{AF100} (%)	χ_{ARM}/χ_{lf} (-)	χ_{ARM}/χ_{fd} (-)	χ_{ARM}/IRM_{100} (10^{-3} mA ⁻¹)	χ_{lf}/IRM_{100} (mA ⁻¹)
MGBC-2021-2-S-T1	34	1.2	226	163	175	6.8	6.8	196	1.4	205
MGBC-2021-2-S-T2	32	1.2	185	137	148	7.1	5.8	151	1.3	231
MGBC-2021-2-S-T3	37	-	200	144	156	7.4	5.4	-	1.4	257
MGBC-2021-2-S-T4	32	0.4	183	137	147	7.0	5.7	445	1.3	236
MGBC-2021-3-S-T1	45	0.8	242	182	201	9.5	5.3	309	1.3	249
MGBC-2021-3-S-T2	41	1.0	215	162	179	9.6	5.3	221	1.3	252
MGBC-2021-3-S-T3	46	0.6	242	179	200	10.3	5.3	376	1.4	254
MGBC-2021-8-S-T1	78	1.8	457	807	863	6.4	5.8	260	0.6	97
MGBC-2021-8-S-T2	78	1.9	430	753	802	6.1	5.5	223	0.6	103
MGBC-2021-8-S-T3	79	1.5	385	766	819	6.4	4.9	254	0.5	103
MGBC-2021-8-S-T4	75	1.4	420	741	791	6.4	5.6	304	0.6	102
MGBC-2021-8-S-T5	82	1.1	370	714	764	6.6	4.5	331	0.5	115
MGBC-2021-8-S-T6	104	0.5	311	719	774	7.1	3.0	692	0.4	144
MGBC-2022-8-D/S-T1	42	0.7	231	-	-	-	5.5	333	-	-
SLM 21-33-S-T1	39	0.4	117	91	101	10.3	3.0	316	1.3	430
MGBC-2022-7-S-T1	45	0.6	178	120	134	10.2	3.9	286	1.5	375
MGBC-2022-7-S-T2	43	0.6	302	-	-	-	7.1	487	-	-
22GOF-8_LAB1	51	1.0	470	175	180	2.8	9.2	453	2.7	293
22GOF-9_LAB1	45	1.0	234	-	-	-	5.3	235	-	-
22GoF-16-1	-	-	194	83	88	5.5	-	-	2.3	-
Spheroidal mean	54	1.0	280	357	384	7.4	5.4	326	1.2	215
SD	21	0.5	106	301	321	2.0	1.4	129	0.6	100
MGBC-2021-4-C-T1	32	0.5	36	34	67	49.1	1.1	69	1.1	930
MGBC-2021-4-C-T2	31	0.4	18	19	58	66.8	0.6	52	1.0	1,600
MGBC-2021-4-C-T3	27	0.5	14	16	60	72.8	0.5	29	0.9	1,644

Table 2
Continued

Sample name	χ_{lf} (10^{-8} m ³ kg ⁻¹)	χ_{fd} (10^{-8} m ³ kg ⁻¹)	χ_{ARM} (10^{-8} m ³ kg ⁻¹)	IRM ₁₀₀ (10^{-5} Am ² kg ⁻¹)	SIRM (10^{-5} Am ² kg ⁻¹)	HIRM _{AF100} (%)	χ_{ARM}/χ_{lf} (-)	χ_{ARM}/χ_{fd} (-)	χ_{ARM}/IRM_{100} (10^{-3} mA ⁻¹)	χ_{lf}/IRM_{100} (mA ⁻¹)
MGBC-2021-11-C-T1	50	1.1	107	520	586	11.3	2.1	98	0.2	95
MGBC-2021-11-C-T2	54	3.2	211	-	-	-	3.9	66	-	-
MGBC-2022-13-C-T1	34	0.5	70	38	51	25.4	2.0	144	1.8	896
MGBC-2022-13-C-T2	39	0.4	191	-	-	-	4.9	469	-	-
Crust mean	38	0.9	92	126	165	45	2.2	132	1.0	1,033
SD	10	1.0	81	221	236	26	1.7	153	0.6	633
SLM 60-D-T1	40	0.3	79	47	76	37.6	2.0	263	1.7	840
SLM 21-35-D-T1	36	0.2	117	81	93	13.7	3.2	472	1.5	449
SLM 21-37-D-T1	42	0.5	118	82	97	15.3	2.8	221	1.4	506
SLM 21-36-D-T1	39	0.3	118	86	100	13.7	3.0	347	1.4	451
MGBC-2022-18-D-T1	28	0.4	45	37	52	28.1	1.6	115	1.2	741
Discoidal mean	37	0.4	96	67	84	22	2.5	284	1.4	598
SD	5	0.1	33	23	20	11	0.7	134	0.2	181
MGBC-2022-7-fluffy	20	0.3	133	83	106	21.7	6.5	381	1.6	246
Total mean	47	0.9	208	255	287	17	4.3	277	1.2	437
SD	19	0.6	128	279	298	19	2.0	152	0.6	422

slightly lower as indicated by lower χ_{ARM} (Table 2). This discrepancy could result from the slower growth of deep ocean Fe-Mn precipitates and an increased terrigenous influence on Baltic Sea concretions, which is attributed to their contrasting marine settings.

Low values of HIRM for spheroidal concretions suggest they are devoid of magnetically hard minerals ($B_{cr} > 100$ mT, such as hematite or goethite), whereas harder minerals (greater HIRM values) are present in crust and discoidal concretions (Figure 3a). Thermomagnetic analyses indicate that in spheroidal samples, subtle susceptibility increases start from $\sim 270^\circ\text{C}$ with a peak at $\sim 300^\circ\text{C}$. A large increase occurs at $\sim 400^\circ\text{C}$ peaking at $\sim 500^\circ\text{C}$ in all morphotypes, followed by a drop across the Curie temperature of magnetite (Figures 4a–4c). These changes in susceptibility may be caused by the conversion of paramagnetic phases into stable Fe phase minerals. Cooling curves are irreversible and indicate the formation of new magnetic materials during heating.

In low-temperature, most of the measured samples display a marked drop in remanence between ca. 10 and 50 K in the FC and ZFC curves (Figures 4d–4p; Figures S3 and S4 in Supporting Information S1). Inflections at around 20 K and sometimes at 35 K could suggest the presence of rhodochrosite with differing Fe and Mn contents and impurities (Frederichs et al., 2003). Rhodochrosite is the most prominent in the spheroidal sample 22GoF-16-1 data (Figure 4g and Figure S3 in Supporting Information S1), which is consistent with the phase having peaks in low-temperature susceptibility in both the in-phase and out of phase components at around 35 K (Figure 4d; Kosterov et al., 2006). Additional evidence for the presence of rhodochrosite is provided by hysteresis loops measured at 25 and 35 K (Figure S5 in Supporting Information S1), revealing a distinct ferrimagnetic component, while at 50 K, the loop predominantly exhibits paramagnetic characteristics (see Kars et al., 2011; Kosterov et al., 2006).

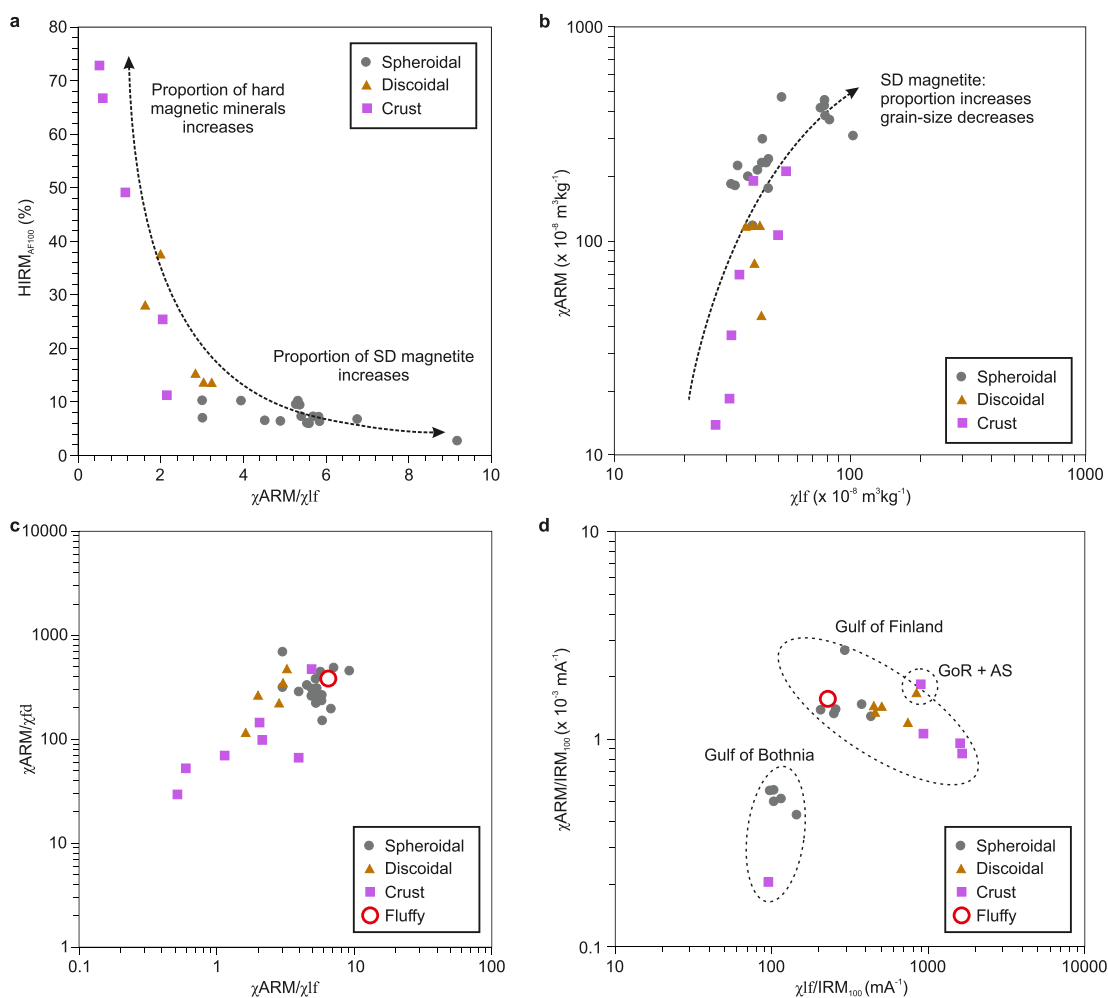


Figure 3. Magnetic properties of the three Baltic Sea Fe-Mn concretion morphotypes. (a) $HIRM_{AF100}$ versus χ_{ARM}/χ_{lf} plot in which the relative magnetic mineral contribution with coercivity (B_{cr}) > 100 mT ($HIRM_{AF100}$) is plotted as a function of the relative amount of single-domain (SD) magnetite (χ_{ARM}/χ_{lf}). (b) χ_{ARM} versus χ_{lf} plot (Banerjee et al., 1981; King et al., 1982), which provides an estimate of magnetite crystal grain size and abundance. (c) Bi-logarithmic plot of χ_{ARM}/χ_{fd} versus χ_{ARM}/χ_{lf} designed to differentiate samples rich in biogenic magnetite from those that contain abundant soil-derived particles (Oldfield, 2013). (d) Biplot of χ_{ARM}/IRM_{100} versus χ_{lf}/IRM_{100} . AS = Archipelago Sea, GoR = Gulf of Riga.

FC-ZFC and RT-SIRM curves further indicate that all the morphotypes contain magnetite (Figures 4e–4p). In contrast to crust and discoidal concretions, however, the spheroidal morphotype shows a double Verwey transition (T_v) at around 100 and 120 K (Figure 4e), which is often associated with a mixture of biogenic and inorganic magnetite, respectively (Chang et al., 2016; Jackson & Moskowitz, 2021). Moreover, crusts and discoidal concretions occasionally have indiscernible or suppressed T_v and two closely aligned curves that converge in magnitude as temperature increases and where FC curves are consistently stronger than ZFC curves (Figures 4i and 4k; Figure S4 in Supporting Information S1). This might suggest a combination of partially oxidized magnetite and goethite, where the contribution from goethite increases as the separation of the curves increase (Dekkers, 1989; Liu et al., 2006; Rochette & Fillion, 1989; Stine et al., 2021; Özdemir & Dunlop, 2010). The humped shape of the RT-SIRM warming and cooling curves, where the hump begins at 300 K and ends at around T_v (~120 K) for some samples (Figures 4h and 4j; Figures S3 and S4 in Supporting Information S1), could further indicate that magnetite is oxidized (Özdemir & Dunlop, 2010).

Spheroidal concretions have clustered high χ_{ARM} and χ_{lf} values that suggest an increased proportion of SD magnetite particles with finer crystal size compared to crust and discoidal concretions (Figure 3b). On the other hand, room temperature χ_{fd} results imply that spheroidal and crust concretions have a higher abundance of superparamagnetic (SP)-sized particles (Table 2). Conventional FORC diagrams indicate domain states that are

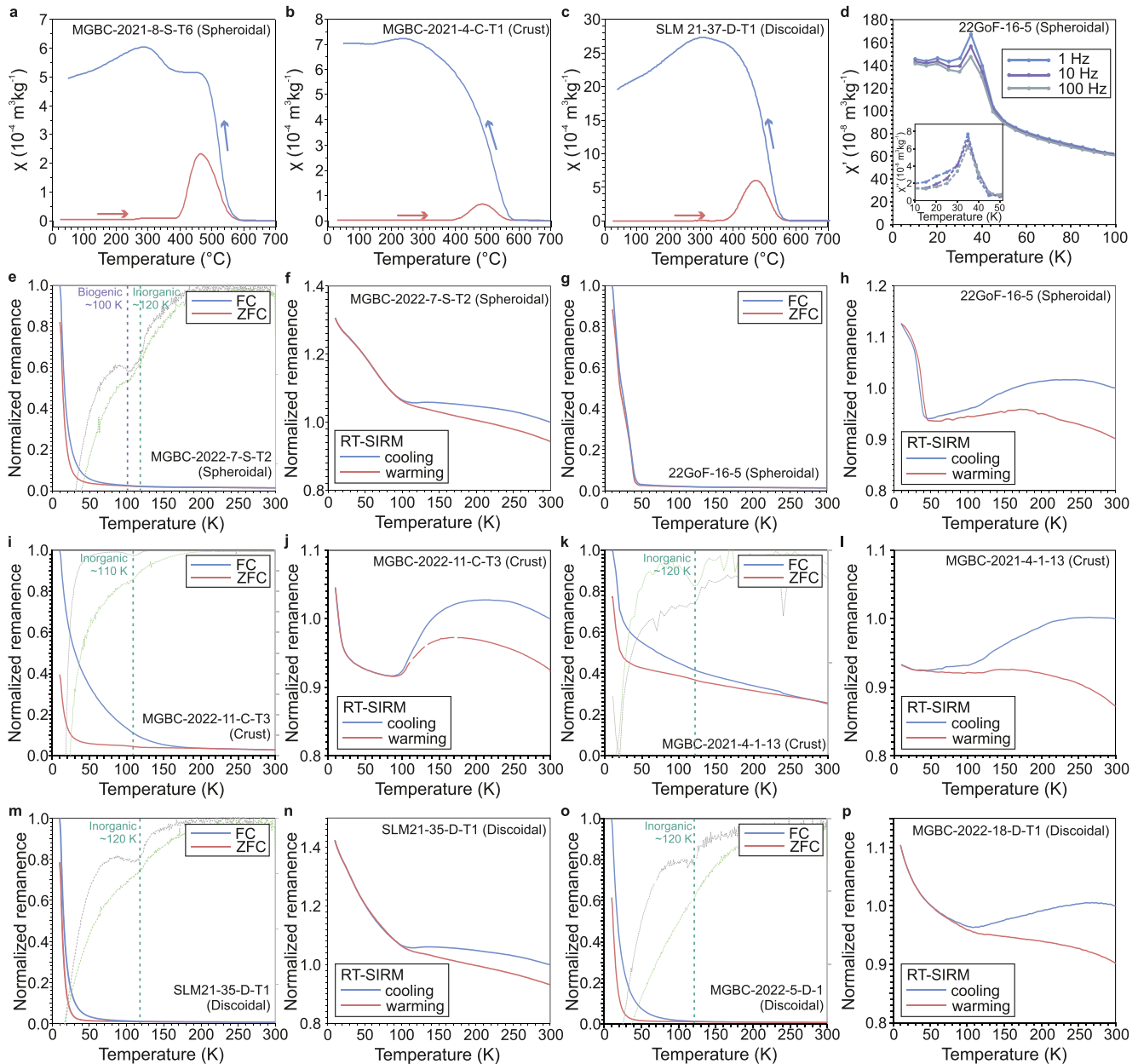


Figure 4. Thermomagnetic analyses of representative Baltic Sea Fe-Mn concretions. (a–c) High temperature χ versus T curves of (a) spheroidal, (b) crust, and (c) discoidal samples. (d) Low temperature in-phase and out-of-phase AC susceptibility for specimen 22GoF-16-1-5. FC and ZFC curves for (e, g) spheroidal (i, k) crust and (m, o) discoidal concretions. Normalized negative second derivatives of FC (dashed green) and ZFC (dashed gray) are indicated for selected samples. (f, h, j, l, n, and p) RT-SIRM warming and cooling curves for the same samples as in (e, g, i, k, m, and o).

consistent with those reported for a combination of SD and vortex states (Figure 5; Figure S8 in Supporting Information S1; cf. Roberts et al., 2019). Additionally, remFORC analyses (Figure S7 in Supporting Information S1) reveal that spheroidal and crust concretions often contain particles near the SP-SD threshold size (Roberts et al., 2019; Zhao et al., 2017), and a central ridge indicative of non-interacting uniaxial SD particles often associated with a biogenic (magnetofossil) origin (Egli et al., 2010; Heslop et al., 2014). In contrast, a bi-logarithmic χ_{ARM}/χ_{fd} versus χ_{ARM}/χ_{lf} plot is consistent with a soil-derived origin (Figure 3c). However, the different morphotypes seem to consist of mixtures, with spheroidal concretions having values closer to those for biogenic magnetite, whereas crust concretions have properties with a closer resemblance to the pedogenic-like endmember. Data for discoidal concretions mainly plot between those for crust and spheroidal concretions. In a

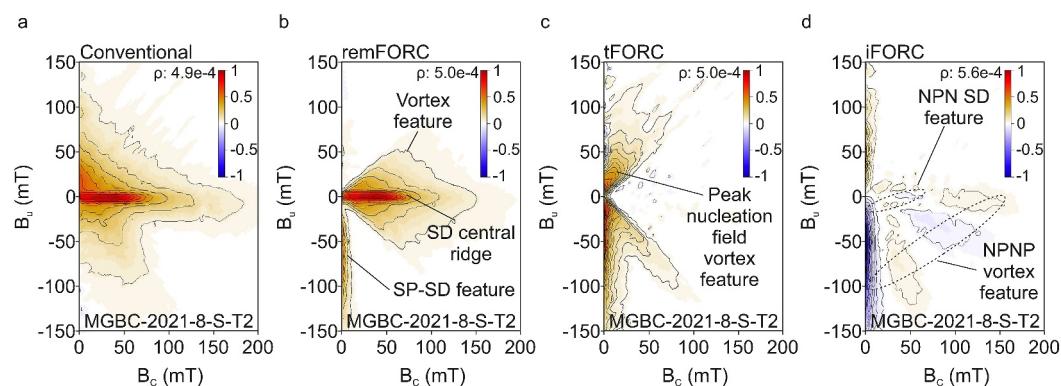


Figure 5. First-order reversal curve (FORC) diagrams (Pike et al., 1999; Roberts et al., 2000) and magnetic domain state diagnosis for a representative spheroidal concretion (MGBC-2021-8-S-T2) from the Bay of Bothnia, Baltic Sea. (a) Conventional FORC diagram where vortex state and noninteracting SD behavior are observed (cf. Roberts et al., 2019). (b) Contributions from magnetic remanence carriers in a remFORC diagram, including a noninteracting SD component, vortex state particles, and a feature along the lower B_u axis produced by a thermally activated component near the SP/SD threshold (Pike et al., 2001; Zhao et al., 2017). (c) A tFORC diagram with evidence for vortex nucleation and annihilation field distributions (Roberts et al., 2017; Zhao et al., 2017). (d) Induced magnetizations in an iFORC diagram, which indicate SD (negative-positive-negative, NPN) and vortex state behavior (negative-positive-negative-positive, NPNP) (Zhao et al., 2017).

χ_{ARM}/IRM_{100} versus χ_{lf}/IRM_{100} biplot, the data segregate into three groups based on location (Gulfs of Bothnia and Finland, and two samples from Gulf of Riga and Archipelago Sea, Figure 3d). In the Gulf of Finland, an inverse relationship between a biogenic magnetite proxy (χ_{ARM}/IRM_{100}) and a bulk concentration proxy (χ_{lf}/IRM_{100}) is observed, where spheroidal concretions have more biogenic characteristics compared to discoidal and crust concretions. The data range and scatter suggest a mixture of SD particles with variable biogenic magnetite contents that depend on the total magnetic mineral concentration. In both plots, the organic-rich mud (MGBC-2022-7-fluffy) that often covers concretion fields has similar properties to spheroidal concretions.

The magnetic properties are supported by TEM and FE-SEM observations of magnetic separates, which indicate the presence of matrix embedded and clustered SP to vortex-sized pedogenic-like particles as well as sporadic isolated Fe oxide crystals, some of which resemble biogenic magnetite (Figure 6). Disaggregation of the putative

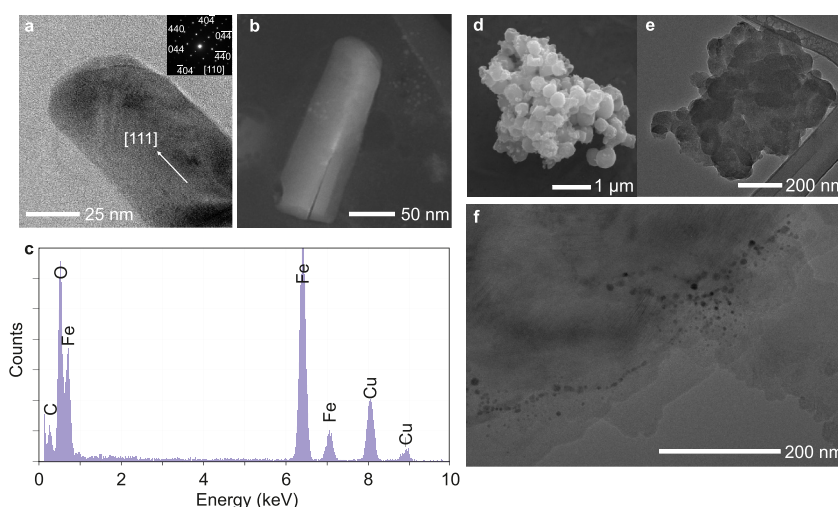


Figure 6. Electron microscope images of a bullet-shaped magnetofossil from a Baltic Sea Fe-Mn concretion. (a) High-resolution TEM image with electron diffraction pattern consistent with magnetite and (b) STEM image of the biogenic magnetite particle. (c) EDS analysis results. Cu originates from the copper TEM grid and C from the carbon film. (d) FE-SEM image of a clump of rounded-hexagonally shaped particles intermixed with spherical particles. (e) Bright-field TEM image of the SD to vortex sized particle clump. (f) Bright-field TEM image of matrix embedded SP-sized particles.

magnetofossils likely occurred during sample preparation. However, the observed distinct bullet shape is typical of marine sedimentary magnetofossils (He & Pan, 2020; Li et al., 2020; Pósfai et al., 2013; Yamazaki & Kawahata, 1998). Both selected area diffraction and EDS analysis suggest that the observed magnetic phase is magnetite (Figure 6). Magnetite magnetofossils are produced by microaerophilic or anaerobic magnetotactic bacteria (MTB) that seem to prefer chemical conditions in the oxic-anoxic transition zone (OATZ) (Flies et al., 2005; Goswami et al., 2022; Kopp & Kirschvink, 2008). These are the first observations of bullet-shaped magnetofossils in Baltic Sea Fe-Mn concretions. Magnetofossils have been reported from polymetallic nodules and Fe-Mn crusts from oligotrophic deep Pacific Ocean and South China Sea environments (Hassan et al., 2020; Jiang et al., 2020; Oda et al., 2018; Yuan et al., 2020). Elongated magnetofossils are absent in such deep ocean concretions, while only bullet-shaped magnetofossils are found here in the Baltic Sea. MTB that produce elongated and bullet-shaped magnetite are thought to live in eutrophic environments (Wagner et al., 2021; Yamazaki & Kawahata, 1998). Growth of bullet-shaped crystals may also be favored by MTB under less oxic conditions, while isotropic crystals are more common under oxic conditions (Chang et al., 2013; Egli, 2004a, 2004b, 2004c; He & Pan, 2020; Usui et al., 2017). Moreover, magnetosomal biomineralization in MTB appears to be intricately regulated, exhibiting a high degree of specificity even at the species level (Li et al., 2020). In general, members of the Nitrospirae phylum or Deltaproteobacteria class tend to synthesize asymmetric crystals, often with kinked or bullet-shaped morphologies. Both Nitrospirae and Deltaproteobacteria have been described in shallow sea Fe-Mn concretions (Shulga et al., 2022; Yli-Hemminki et al., 2014).

3.2. Microstructure and Origin of Magnetization in Two Fe-Mn Concretions From the Gulf of Finland

Baltic Sea Fe-Mn concretions are mainly composed of amorphous Fe-Mn (oxyhydr)oxide masses with occasional cemented micron- to submicron-scale crystals (Figures 7a and 7b), which often include Al- and Si-containing detrital minerals. Two representative concretions (MGBC-2021-4-1 and 22GoF-16-1) have similar microstructural features with variable primary growth patterns, including laminated, columnar, massive, and mottled structures, often accompanied by structural discontinuities (Figures 7c–7j). Comparing the results of μ CT scans and μ XRF element mapping reveals that the densest growth zones generally have a high Fe concentration, while Mn-rich zones have lower density (Figure 8). Specifically, sample 22GoF-16-1 is composed primarily of Mn phases, whereas sample MGBC-2021-4-1 has a higher Fe content. In most cases, Fe-rich zones have laminated and massive structures with occasional Mn mottles. In contrast, Mn-rich zones have predominantly columnar structures with stromatolitic and dendritic textures. Notably, sample MGBC-2021-4-1 contains a significant detrital mineral content with variable grain sizes embedded within the Fe-Mn matrix, while sample 22GoF-16-1 has limited detrital material (Figures S9 and S10 in Supporting Information S1).

Based on the microstructure and chemical composition, multiple growth phases can be distinguished within the examined concretions. The spheroidal concretion (sample 22GoF-16-1) has irregular concentric Mn-rich growth bands interbedded with sporadic, thin, and fragmentary Fe-rich laminae (Figure 8; Figure S9 in Supporting Information S1). Magnetic measurements indicate that rhodochrosite may be present in addition to magnetite (Figure 4; Figures S3 and S5 in Supporting Information S1). Formation of rhodochrosite-containing concretions requires specific conditions: (a) high alkalinity and (b) elevated pore water Mn^{2+} concentrations. Rhodochrosite is sensitive to redox changes and can readily oxidize to Mn (oxyhydr)oxides via various abiotic and biotic processes, which are often heterogeneous and produce mixed Mn oxides (Namgung & Lee, 2021). Importantly, Mn-carbonates can be protected from complete dissolution by (oxyhydr)oxide surface patinas that form under oxic conditions above pH 7.7 (Duckworth & Martin, 2004). While rhodochrosite is not diagnostic of the diagenetic environment (non-sulfidic vs. sulfidic (Berner, 1981)), the prolonged influence of sulfidic pore waters during concretion formation can be considered unlikely because Fe oxides and hydroxides are highly reactive under sulfidic diagenetic conditions (Roberts, 2015). The possible occurrence of rhodochrosite throughout the concretion growth process reflects diagenetic Mn cycling as an important factor for spheroidal concretion formation in deeper parts of the Baltic Sea.

The mixed crust-discoidal concretion (sample MGBC-2021-4-1) contains a complex combination of structural discontinuities and alternating Fe and Mn-rich growth bands (Figure 8; Figure S10 in Supporting Information S1). Fe-rich bands have elevated P content, are typically dense and laminated (occasionally massive) and are mostly devoid of detrital material, although they may contain crack-type discontinuities with occasional Mn oxide mottles and sporadic siliciclastic grains (Figure S10 in Supporting Information S1). In contrast, Mn-rich zones are

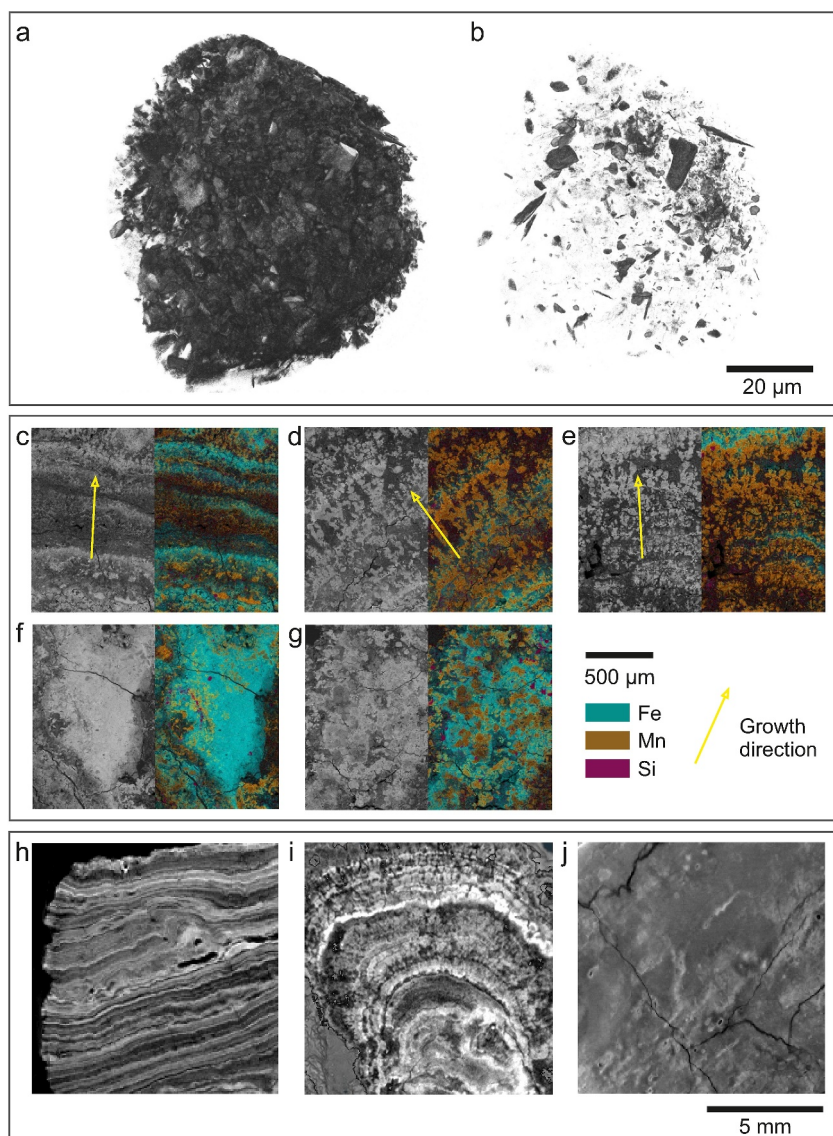


Figure 7. Microstructural characteristics of Baltic Sea Fe-Mn concretions: NanoCT images of (a) Fe-Mn matrix in the concretions and (b) matrix embedded crystals. (c–g) FE-SEM BSE (left) and EDS element mapping of Fe, Mn, and Si (right) and (h–j) μ CT images of structural elements in the concretions. Concretion microstructures: laminated (c, h), columnar (d–e and i), massive (f, j), and mottled (g). Growth direction is indicated by the yellow arrows.

more porous with columnar growth structures that often cement fine-grained Al- and Si-rich detrital minerals (Figure 9b; Figure S10 in Supporting Information S1).

These relationships are also reflected in magnetic properties, where zones with increased detrital material also contain elevated proportions of coarser magnetic minerals (Figures 9d and 9f; Figures S6 and S7 in Supporting Information S1). Coercivity spectra unmixing suggests that magnetic mineral sub-populations in the concretions can be best explained by two to three components: a low coercivity widely dispersed component (B_h : 8–37 mT, mean 22 mT; DP: 0.35–0.50, mean 0.42), a medium coercivity component with narrow dispersion (B_h : 44–93 mT, mean 62 mT; DP: 0.17–0.27, mean 0.21), and a high coercivity component (B_h : 115–756 mT, mean 339 mT; DP: 0.29–0.86, mean 0.53) (Figures 9c and 9d). The first component has coercivity and dispersion consistent with detrital magnetite (Egli, 2003; Lasco & Plank, 2013; Maxbauer et al., 2016; Ohenhen et al., 2022), while the second component aligns with the tightly dispersed biogenic soft (BS) and biogenic hard (BH) components described by Egli (2004a, 2004b, 2004c). The BS component is often associated with equant magnetofossils,

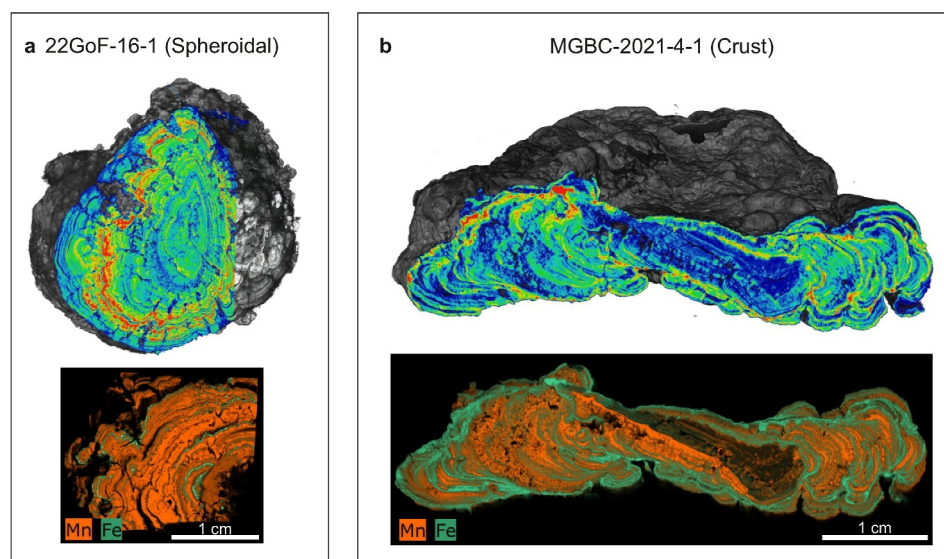


Figure 8. Internal structure of Fe-Mn concretions from μ CT reconstructions (top images) and Fe-Mn composition from μ XRF element mapping (bottom images) of (a) a spheroidal concretion (22GoF-16-1) and (b) a crust concretion (MGBC-2021-4-1). The color scheme indicates density changes from less dense (blue) to more dense (red).

whereas the BH component is typical of elongated and bullet-shaped magnetofossils (e.g., Wagner et al., 2021; Yamazaki et al., 2020). In most specimens, the coercivity of component 2 is somewhat larger than that of BS but within or slightly below the values typical of BH. This variation may be caused by complete magnetofossil oxidation under oxic conditions, inconsistent strand configurations, or variable axial ratios for bullet-shaped magnetofossils (Amor et al., 2022; Ge et al., 2014; Usui et al., 2017; Yamazaki et al., 2020). The presence of multistranded and/or fold-collapsed chains is corroborated by a FORC diagram for the spheroidal concretion (22GoF-16-1). Oval contours surrounding the central ridge (Figure 9e) are similar to those produced in simulations by Amor et al. (2022) for similar chain configurations. The third component is a magnetically hard mineral, likely goethite, suggested by low-temperature measurements. From the magnetic properties, biogenic magnetite is most prominently present in the spheroidal concretion, while the crust-like concretion has an increased detrital contribution.

3.3. Implications for the Hydrodynamic and Depositional Environment

The composition and internal structure of the examined Fe-Mn concretions imply that they formed via several distinct stages. Early growth was by Fe-Mn oxide cementation of the substrate, followed by development of chaotic columnar and dendritic growth patterns, sometimes as larger lobes or botryoids, especially in the spheroidal morphotype. Previous research suggests that columnar structures are typical in environments with reduced hydrodynamic activity and rapid growth rates, whereas dendritic growth patterns may result from inconsistent growth on varied locations on the same surface (Ren et al., 2023). Inconsistent growth may be caused by several factors such as physical barriers formed by trapped detrital mineral grains, and bioturbation or other subtle movements and rotations during concretion formation. Subsequent alternating lamellar and columnar growth phases become apparent. Lamellar growth is indicative of weaker bottom currents and oxidation conditions, while laminae with Mn mottles are likely to reflect a more energetic and turbulent seawater environment (Guan et al., 2017). Growth structures that reflect a more energetic environment also appear to contain more detrital material, as evidenced by FE-SEM imaging, μ XRF mapping, and magnetic properties of these growth zones (Figures 7–9; Supporting Information S1). Concretions from shallower waters closer to shore have increased terrigenous influences. Spheroidal concretions seem to contain more columnar structures, which suggests that they generally form in more tranquil settings with comparatively rapid growth compared to crust concretions. $^{226}\text{Ra}/\text{Ba}$ and ^{210}Pb radiometric dating of Baltic Sea Fe-Mn concretions support more rapid spheroidal than crust concretion growth (Grigoriev et al., 2013; Liebetrau et al., 2002).

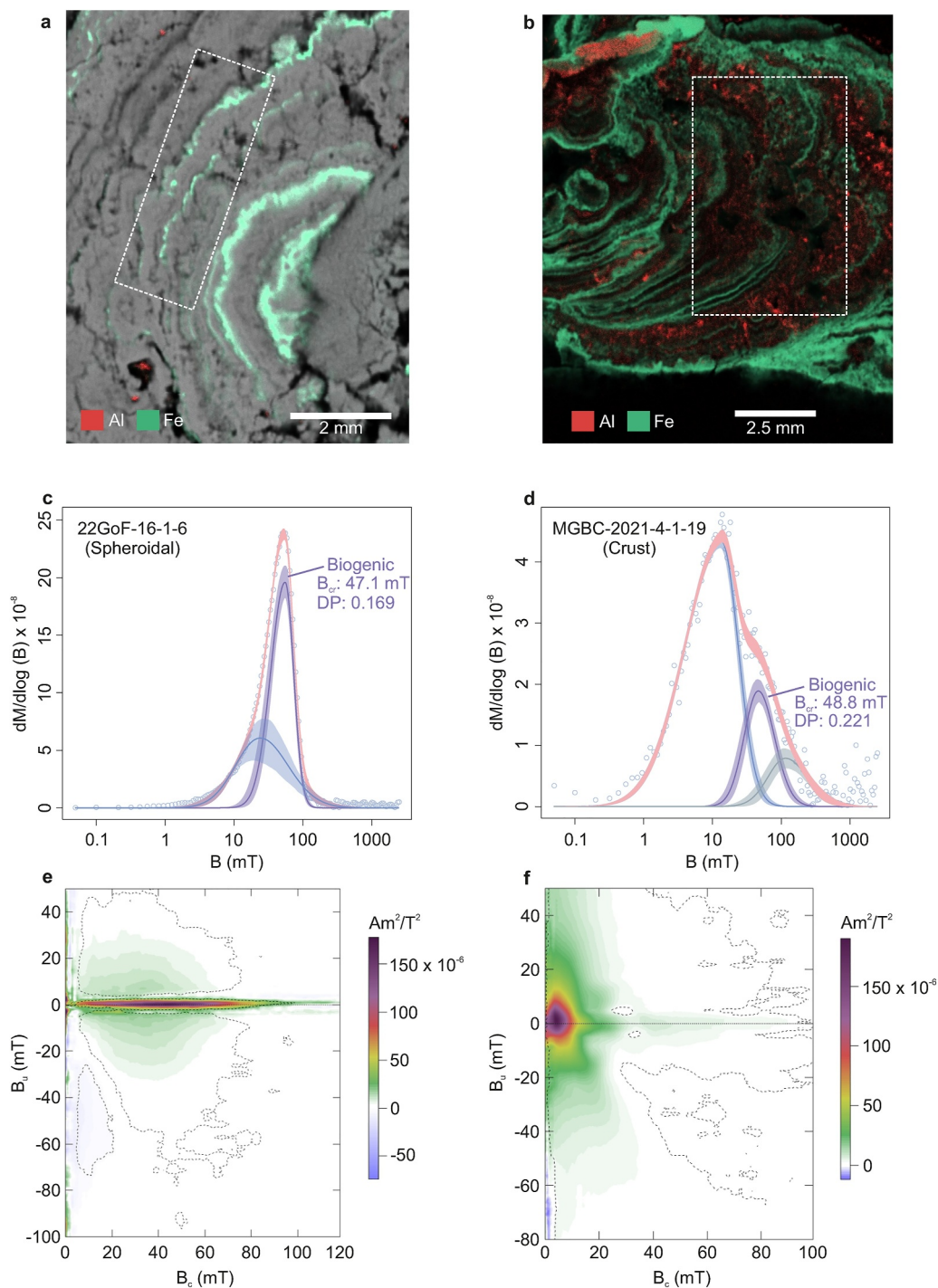


Figure 9. Comparison of microstructural and magnetic features of spheroidal (22GoF-16-1) and crust (MGBC-2021-4-1) concretions from the Gulf of Finland. (a, b) μ XRF element maps of Fe and Al contents. White dotted boxes are approximate areas from which representative specimens were taken for magnetic analyses, as presented in (c–f). (c, d) Coercivity spectra unmixing for (c) a spheroidal concretion with a minor detrital component and a predominant biogenic component while (d) is for a crust concretion dominated by a detrital component with a minor biogenic component, and a high coercivity third component, likely goethite. (e, f) Conventional FORC diagrams for representative specimens. (e) The spheroidal sample is dominated by non-interacting SD particles while (f) the crust sample contains coarser magnetic particles.

Given that MTB may be the source of nanoscale SD magnetite in Baltic Sea Fe-Mn concretions, as discussed above, it appears that both spheroidal morphotype formation conditions and increased water depth favor MTB activity and the production and/or preservation of biogenic magnetite (Tables 1 and 2, Figure 3). Enhanced MTB activity could be linked to the expanding influence of oxygen deficient zones in concretion-forming areas, as increasing water depth and Mn content are usually associated with Mn-reducing conditions, especially in waters deeper than 80 m (Force & Cannon, 1988; Huckriede & Meischner, 1996; Lenz et al., 2015). The presence of rhodochrosite in spheroidal concretion 22GoF-16-1 supports this hypothesis because it forms during sedimentary reductive diagenesis in both suboxic (manganous) and anoxic sulfidic settings (Berner, 1981; Glasby & Schulz, 1999). Rhodochrosite is also typical in rapidly deposited fine-grained organic-rich sediments where carbonate forms via CO₂ production during oxidation of organic matter coupled to Mn oxyhydroxide reduction (Glasby & Schulz, 1999). Organic matter content is, in turn, higher in areas where spheroidal concretions form thick layers with at least ~80% surface coverage, and is considered to be connected to bacterial activity (Zhamoïda et al., 2007). While Baltic Sea concretions generally grow in well-oxygenated bottom waters, expanding hypoxic-anoxic zones favored by MTB likely result in higher biogenic particle proportions in this morphotype under such conditions. Growth areas of spheroidal concretions are also likely to be chemically conducive to magnetofossil preservation. In most cases, sustained oxygen-rich conditions inhibit magnetite biomineralization (Liu et al., 2010; Roberts et al., 2011). Conversely, continuous reducing diagenetic conditions facilitate biogenic magnetite dissolution (e.g., Roberts, 2015). Elongated and bullet-shaped magnetofossils are generally slightly more resistant to reductive diagenesis than equant magnetofossils (Rodelli et al., 2019).

Yuan et al. (2020) proposed that MTB thrive on deep ocean hydrogenetic crust surfaces. These crusts form due to inorganic precipitation of colloidal Fe-Mn oxyhydroxides which leads to localized oxygen deficiency. As Fe-Mn crusts grow, they gradually encrust falling marine debris, including fine plankton particles, which subsequently corrode and dissolve. This process fosters development of a microaerophilic environment on crust surfaces that are suitable for MTB. In the Baltic Sea, spheroidal concretions are thought to form where Mn, Fe, and associated building materials remobilize from underlying sediments and/or migrate laterally from peripheral anoxic mud zones to oxygenated bottom waters where concretions form (Emelyanov, 2004; Ingri & Pontér, 1986; Winterhalter, 1980; Zhamoïda et al., 2017). Thus, a further MTB source in the Baltic Sea could be the oxygen-deficient zones adjacent to oxygen-rich concretion formation areas, from which living or dead MTB cells may be transported by bottom currents and/or within the flowing fluffy organic-rich mud layer that commonly covers concretion fields. This scenario is consistent with a proposed alternative magnetofossil origin in deep ocean crusts (Oda et al., 2018). While encrustation under oxidizing conditions leads to gradual magnetite oxidation, as suggested by our low-temperature data, biogenic magnetite remains detectable from its magnetic properties and distinctive crystal morphologies and sizes despite oxidation (Chang et al., 2013; Rodelli et al., 2018).

This magnetofossil accumulation method in Baltic Sea concretions is supported by their likely presence in the flowing fluffy and organic-rich mud observed across multiple study sites (Figures 3c, 3d, and 10). Component unmixing suggests a detrital, prominent biogenic, and a high coercivity component, while the narrow central ridge coupled with the vertical spread and strong divergence toward $B_c = 0$ mT in the FORC diagram implies that the fluffy mud contains a combination of SD and coarse (possibly multi domain) magnetic particles (Figures 10a and 10b). While the fluffy mud has similar bulk magnetic properties to spheroidal concretions (Figures 3c and 3d), it also has a double T_v at ~100 and 120 K in the FC-ZFC curves, which indicates the presence of both biogenic and inorganic magnetite (Figure 10c). A clear T_v is also observed in the RT-SIRM curves (Figure 10d).

During periods of abundant Mn precipitation, these concretions are likely partially or completely buried within the flowing fluffy layer, with a redox front forming at the water-mud interface. Pore water Mn beneath the studied Fe-Mn concretions may diffuse and concentrate at the interface where Mn oxide formation occurs, possibly catalyzed by poorly crystalline Fe oxides (Davies & Morgan, 1989) and/or bacterial processes (Yu & Leadbetter, 2020). If spheroidal concretions experience such conditions more than the other two morphotypes, it could partly account for the prominent biogenic magnetite-like signature rapidly growing Mn-rich spheroidal concretions. Moreover, the observed inverse relationship between χ_{ARM}/IRM_{100} and χ_{lf}/IRM_{100} (Figure 3d) may imply that biogenic magnetite formation occurs in situ within an environment where biological formation of secondary magnetite particles contends with abiogenic or biologically induced pathways. These pathways contribute to precipitation of magnetite particles that are either isolated or clustered (Figures 6d–6f), with properties reminiscent of pedogenic magnetite. It is also possible that the distinct geographical differences may be

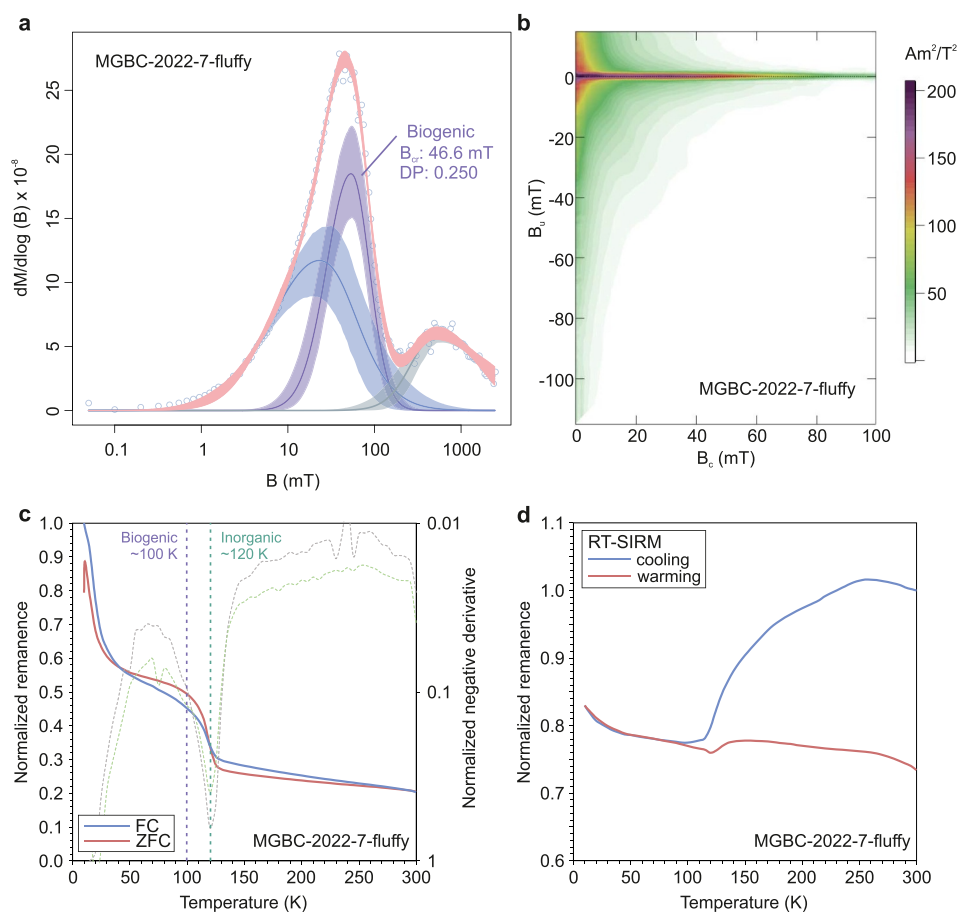


Figure 10. Coercivity spectra component unmixing and conventional FORC diagram for a sample of fluffy, organic-rich mud that often covers Fe-Mn concretions as a thin layer on the Baltic seafloor. (a) Component unmixing suggests the presence of three components: low coercivity detrital magnetite, medium coercivity biogenic magnetite, and a high coercivity component, possibly detrital hematite. (b) A conventional FORC diagram for the sample is indicative of a mixture of coarse-grained (likely MD) particles and uniaxial noninteracting SD magnetite. (c) FC-ZFC curves and normalized negative derivative of FC (green line) indicating double Verwey transition (T_v) at ~ 100 and ~ 120 K and a faint Morin transition (T_m) for hematite at ~ 260 K. (d) RT-SIRM warming and cooling curves.

related to locally variable erosional inputs, geochemical conditions, and/or salinity differences. Salinity has been suggested to control MTB diversity (Lin et al., 2012).

The possible presence of bullet-shaped magnetofossils in coastal Baltic Sea concretions suggests that a more eutrophic environment, compared to the oligotrophic conditions associated with deep ocean concretions, facilitates the formation of elongated magnetosomal magnetite. Magnetofossil abundance could, in turn, serve as an indicator of shelf sea eutrophication intensity and hypoxic-anoxic zone prevalence. Oxygen deficiency in shelf sea regions has expanded in recent decades and is expected to intensify in the future due to global warming and other human-induced activities (Breitburg et al., 2018). Although the Baltic Sea is generally considered a mesotrophic ecosystem, recent anthropogenic activities have led to increased nutrient load from rivers and atmospheric deposition that has enhanced ecosystem productivity (Kuliński et al., 2022). Moreover, magnetofossils appear to be common in both shallow water and deep ocean Fe-Mn concretions when conditions conducive to MTB metabolism are met, and they likely contribute to the remanent magnetization of these deposits on a global scale.

4. Conclusions

We report here the magnetic characteristics, microstructure, and origin of Baltic Sea Fe-Mn concretions, which shed light on their formation processes and environmental implications. Spheroidal concretions are prevalent in

many parts of the coastal Baltic Sea and contain a higher proportion of fine-grained magnetite likely originating from biogenic processes. The putative presence of bullet-shaped magnetofossils produced by magnetotactic bacteria hints at a eutrophic and less oxic formation environments, as supported by the possible presence of rhodochrosite, which indicates diagenetic Mn release from surrounding sediments, especially in deeper water settings. In contrast, crust and discoidal concretions in shallower waters contain higher proportions of pedogenic-like and detrital (including magnetically hard) minerals with variable grain sizes. This reflects an increased continental influence compared to spheroidal concretions. Furthermore, it suggests an intricate interaction between biological processes that regulate secondary magnetite formation and competing pathways, whether abiogenic or biologically induced, which influence the processes governing Fe-Mn concretion formation in the Baltic Sea. Microstructural analysis of the concretions revealed multiple growth stages, with laminated, columnar, and dendritic structures indicating varying hydrodynamic and depositional conditions. In general, spheroidal concretions seem to form in more tranquil settings compared to discoidal and crust concretions.

Our results provide insights into the complex interplay of environmental conditions, biogenic processes, and mineralogical composition that influence Fe-Mn concretion growth and magnetic properties in the Baltic Sea. Moreover, biogenic magnetite will contribute to the remanent magnetization of Baltic Sea Fe-Mn concretions. Further research in this area should enhance the knowledge of biomineralization processes and their implications for biogenic magnetite preservation.

Data Availability Statement

Magnetic data are deposited in the MagIC database (Wasiljeff et al., 2024) and computed tomography data at Fairdata (Wasiljeff & Kuva, 2022).

Acknowledgments

We acknowledge the captains and crews of RV *Geomari* and *Electra* for coring and sampling assistance. We thank Yao Qian for help with MPMS measurements at ANU, Felipe Kremer (CAM, ANU) for invaluable assistance with TEM imaging, and Ramon Egli and Jinhua Li for constructive feedback. This work was supported by the Research Council of Finland (Fermaid project, Grant 332249), and the Australian Research Council (DP200100765). W.-L.H. acknowledges financial support from the Swedish Research Council, Vetenskapsrådet (VR), through the project “Cryosphere-driven submarine groundwater in the Arctic” (Project No: 2021-04962). A.H. was supported by Estonian Research Council Grant PRG1993. Part of this work was performed as a Visiting Fellow at the Institute for Rock Magnetism (IRM), University of Minnesota. The IRM is a U. S. National Multi-user Facility supported through the Instrumentation and Facilities program of the National Science Foundation (NSF EAR-2153786), and by funding from the University of Minnesota. This study also used research facilities provided by the Finnish Marine Research Infrastructure (FINMARI) network and micro-XRF by the Research Council of Finland via the RAMI infrastructure project (Grant 337560).

References

- Amor, M., Wan, J., Egli, R., Carlu, J., Gatel, C., Andersen, I. M., et al. (2022). Key signatures of magnetofossils elucidated by mutant magnetotactic bacteria and micromagnetic calculations. *Journal of Geophysical Research: Solid Earth*, 127(1), e2021JB023239. <https://doi.org/10.1029/2021JB023239>
- Axelsson, M. D., Rodushkin, I., Baxter, D. C., Ingri, J., & Öhlander, B. (2002). High spatial resolution analysis of ferromanganese concretions by LA-ICP-MS. *Geochemical Transactions*, 3(1), 40. <https://doi.org/10.1186/1467-4866-3-40>
- Banerjee, S. K., King, J., & Marvin, J. (1981). A rapid method for magnetic granulometry with applications to environmental studies. *Geophysical Research Letters*, 8(4), 333–336. <https://doi.org/10.1029/GL008i004p00333>
- Baturin, G. (2010). Element composition of ferromanganese concretions in the Black Sea. *Oceanology*, 50(1), 83–92. <https://doi.org/10.1134/S0001437010010108>
- Berner, R. A. (1981). A new geochemical classification of sedimentary environments. *Journal of Sedimentary Research*, 51. <https://doi.org/10.1306/212F7C7F-2B24-11D7-8648000102C1865D>
- Breitbart, D., Levin, L. A., Oschlies, A., Grégoire, M., Chavez, F. P., Conley, D. J., et al. (2018). Declining oxygen in the global ocean and coastal waters. *Science*, 359(6371), eaam7240. <https://doi.org/10.1126/science.aam7240>
- Callender, E., & Bowser, C. J. (1976). Freshwater ferromanganese deposits. In K. H. Wolf, U. Au, M. Fe, S. W. Hg, & P. Deposits (Eds.), *Handbook of strata-bound and stratiform ore deposits* (pp. 341–394). Elsevier. <https://doi.org/10.1016/B978-0-444-41407-6.50011-8>
- Chan, L. S., Chu, C. L., & Ku, T. L. (1985). Magnetic stratigraphy observed in ferromanganese crust. *Geophysical Journal International*, 80(3), 715–723. <https://doi.org/10.1111/j.1365-246x.1985.tb05120.x>
- Chang, L., Heslop, D., Roberts, A. P., Rey, D., & Mohamed, K. J. (2016). Discrimination of biogenic and detrital magnetite through a double Verwey transition temperature. *Journal of Geophysical Research: Solid Earth*, 121(1), 3–14. <https://doi.org/10.1002/2015JB012485>
- Chang, L., Winklhofer, M., Roberts, A. P., Heslop, D., Florindo, F., Dekkers, M. J., et al. (2013). Low-temperature magnetic properties of pelagic carbonates: Oxidation of biogenic magnetite and identification of magnetosome chains. *Journal of Geophysical Research: Solid Earth*, 118(12), 6049–6065. <https://doi.org/10.1002/2013JB010381>
- Crecelius, E. A., Carpenter, R., & Merrill, R. T. (1973). Magnetism and magnetic reversals in ferromanganese nodules. *Earth and Planetary Science Letters*, 17(2), 391–396. [https://doi.org/10.1016/0012-821X\(73\)90206-9](https://doi.org/10.1016/0012-821X(73)90206-9)
- Davies, S. H. R., & Morgan, J. J. (1989). Manganese(II) oxidation kinetics on metal oxide surfaces. *Journal of Colloid and Interface Science*, 129(1), 63–77. [https://doi.org/10.1016/0021-9797\(89\)90416-5](https://doi.org/10.1016/0021-9797(89)90416-5)
- Dekkers, M. J. (1989). Magnetic properties of natural Goethite-II. Trm behaviour during thermal and alternating field demagnetization and low-temperature treatment. *Geophysical Journal International*, 97(2), 341–355. <https://doi.org/10.1111/j.1365-246X.1989.tb00505.x>
- Duckworth, O. W., & Martin, S. T. (2004). Role of molecular oxygen in the dissolution of siderite and rhodochrosite. *Geochimica et Cosmochimica Acta*, 68(3), 607–621. [https://doi.org/10.1016/S0016-7037\(03\)00464-2](https://doi.org/10.1016/S0016-7037(03)00464-2)
- Egli, R. (2003). Analysis of the field dependence of remanent magnetization curves. *Journal of Geophysical Research*, 108(B2). <https://doi.org/10.1029/2002JB002023>
- Egli, R. (2004a). Characterization of individual rock magnetic components by analysis of remanence curves, 1. Unmixing natural sediments. *Studia Geophysica et Geodaetica*, 48(2), 391–446. <https://doi.org/10.1023/B:SGEG.0000020839.45304.6d>
- Egli, R. (2004b). Characterization of individual rock magnetic components by analysis of remanence curves: 2. Fundamental properties of coercivity distributions. *Physics and Chemistry of the Earth*, 29(13–14), 851–867. <https://doi.org/10.1016/j.pce.2004.04.001>
- Egli, R. (2004c). Characterization of individual rock magnetic components by analysis of remanence curves: 3. Bacterial magnetite and natural processes in lakes. *Physics and Chemistry of the Earth*, 29(13–14), 869–884. <https://doi.org/10.1016/j.pce.2004.03.010>

- Egli, R. (2013). VARIFORC: An optimized protocol for calculating non-regular first-order reversal curve (FORC) diagrams. *Global and Planetary Change*, *110*, 302–320. <https://doi.org/10.1016/j.gloplacha.2013.08.003>
- Egli, R., Chen, A. P., Winkhofer, M., Kodama, K. P., & Horng, C.-S. (2010). Detection of noninteracting single domain particles using first-order reversal curve diagrams. *Geochemistry, Geophysics, Geosystems*, *11*(1). <https://doi.org/10.1029/2009GC002916>
- Emelyanov, E. M. (2004). The Baltic deep as a model for explaining iron and manganese ore formation. *Zeitschr Angewand Geol Sonderh*, *2*(2), 161–176.
- Flies, C. B., Jonkers, H. M., de Beer, D., Bosselmann, K., Böttcher, M. E., & Schöler, D. (2005). Diversity and vertical distribution of magnetotactic bacteria along chemical gradients in freshwater microcosms. *FEMS Microbiology Ecology*, *52*(2), 185–195. <https://doi.org/10.1016/j.femsec.2004.11.006>
- Force, E. R., & Cannon, W. F. (1988). Depositional model for shallow-marine manganese deposits around Black Shale basins. *Economic Geology*, *83*(1), 93–117. <https://doi.org/10.2113/gsecongeo.83.1.93>
- Frank, M., O'Nions, R. K., Hein, J. R., & Banakar, V. K. (1999). 60 Myr records of major elements and Pb–Nd isotopes from hydrogenous ferromanganese crusts: Reconstruction of seawater paleochemistry. *Geochimica et Cosmochimica Acta*, *63*(11–12), 1689–1708. [https://doi.org/10.1016/S0016-7037\(99\)00079-4](https://doi.org/10.1016/S0016-7037(99)00079-4)
- Frederichs, T., von Dobeneck, T., Bleil, U., & Dekkers, M. J. (2003). Towards the identification of siderite, rhodochrosite, and vivianite in sediments by their low-temperature magnetic properties. *Physics and Chemistry of the Earth*, *28*(16–19), 669–679. [https://doi.org/10.1016/S1474-7065\(03\)00121-9](https://doi.org/10.1016/S1474-7065(03)00121-9)
- Gasparatos, D., Tarenidis, D., Haidouti, C., & Oikonomou, G. (2005). Microscopic structure of soil Fe–Mn nodules: Environmental implication. *Environmental Chemistry Letters*, *2*(4), 175–178. <https://doi.org/10.1007/s10311-004-0092-5>
- Ge, K., Williams, W., Liu, Q., & Yu, Y. (2014). Effects of the core-shell structure on the magnetic properties of partially oxidized magnetite grains: Experimental and micromagnetic investigations. *Geochemistry, Geophysics, Geosystems*, *15*(5), 2021–2038. <https://doi.org/10.1002/2014GC005265>
- Glasby, G. P., Emelyanov, E. M., Zhamoïda, V. A., Baturin, G. N., Leipe, T., Bahlo, R., & Bonacker, P. (1997). Environments of formation of ferromanganese concretions in the Baltic Sea: A critical review. *Geological Society, London, Special Publications*, *119*(1), 213–237. <https://doi.org/10.1144/GSL.SP.1997.119.01.14>
- Glasby, G. P., & Schulz, H. D. (1999). Eh pH Diagrams for Mn, Fe, Co, Ni, Cu and As under seawater conditions: Application of two new types of Eh pH diagrams to the study of specific problems in marine geochemistry. *Aquatic Geochemistry*, *5*(3), 227–248. <https://doi.org/10.1023/A:1009663322718>
- González, F. J., Somoza, L., Lunar, R., Martínez-Frías, J., Rubí, J. A. M., Torres, T., et al. (2010). Internal features, mineralogy and geochemistry of ferromanganese nodules from the Gulf of Cadiz: The role of the Mediterranean Outflow Water undercurrent. *Journal of Marine Systems*, *80*(3–4), 203–218. <https://doi.org/10.1016/j.jmarsys.2009.10.010>
- Goswami, P., He, K., Li, J., Pan, Y., Roberts, A. P., & Lin, W. (2022). Magnetotactic bacteria and magnetofossils: Ecology, evolution and environmental implications. *Npj Biofilms Microbiomes*, *8*, 1–14. <https://doi.org/10.1038/s41522-022-00304-0>
- Grewingk, C. (1884). *Submarine exposure of eastern Baltic dolomite* (Vol. 6, pp. 83–87). Sitzungsberichte Naturforscher-Gesellschaft Univ. Dorpat. (in German).
- Grigoriev, A. G., Zhamoïda, V. A., Gruzdov, K. A., & Krymsky, R. S. (2013). Age and growth rates of ferromanganese concretions from the Gulf of Finland derived from 210Pb measurements. *Oceanology*, *53*(3), 345–351. <https://doi.org/10.1134/S0001437013030041>
- Guan, Y., Sun, X., Ren, Y., & Jiang, X. (2017). Mineralogy, geochemistry and genesis of the polymetallic crusts and nodules from the South China Sea. *Ore Geology Reviews*, *89*, 206–227. <https://doi.org/10.1016/j.oregeorev.2017.06.020>
- Hannington, M., Petersen, S., & Krätschell, A. (2017). Subsea mining moves closer to shore. *Nature Geoscience*, *10*(3), 158–159. <https://doi.org/10.1038/ngeo2897>
- Harrison, R. J., & Feinberg, J. M. (2008). FORCinel: An improved algorithm for calculating first-order reversal curve distributions using locally weighted regression smoothing. *Geochemistry, Geophysics, Geosystems*, *9*(5). <https://doi.org/10.1029/2008GC001987>
- Hassan, M. B., Rodelli, D., Benites, M., Abreu, F., Murton, B., & Jovane, L. (2020). Presence of biogenic magnetite in ferromanganese nodules. *Environ. Microbiol. Rep.*, *12*(3), 288–295. <https://doi.org/10.1111/1758-2229.12831>
- He, K., & Pan, Y. (2020). Magnetofossil abundance and diversity as paleoenvironmental proxies: A case study from southwest Iberian Margin sediments. *Geophysical Research Letters*, *47*(8), e2020GL087165. <https://doi.org/10.1029/2020GL087165>
- Hein, J. R., Koschinsky, A., & Kuhn, T. (2020). Deep-ocean polymetallic nodules as a resource for critical materials. *Nature Reviews Earth & Environment*, *1*(3), 158–169. <https://doi.org/10.1038/s43017-020-0027-0>
- Heslop, D., Roberts, A. P., & Chang, L. (2014). Characterizing magnetofossils from first-order reversal curve (FORC) central ridge signatures. *Geochemistry, Geophysics, Geosystems*, *15*(6), 2170–2179. <https://doi.org/10.1002/2014GC005291>
- Hessle, C. (1924). Evaluation of the bottom deposits of the inner Baltic Sea. *Meddelanden fran Kungliga Lantbruksstyrelsen*, *250*, 1–52. (in Swedish).
- Hu, P. X., Zhao, X., Roberts, A. P., Heslop, D., & Viscarra Rossel, R. A. (2018). Magnetic domain state diagnosis in soils, loess, and marine sediments from multiple first-order reversal curve-type diagrams. *Journal of Geophysical Research: Solid Earth*, *123*(2), 998–1017. <https://doi.org/10.1002/2017JB015195>
- Huckriede, H., & Meischner, D. (1996). Origin and environment of manganese-rich sediments within black-shale basins. *Geochimica et Cosmochimica Acta*, *60*(8), 1399–1413. [https://doi.org/10.1016/0016-7037\(96\)00008-7](https://doi.org/10.1016/0016-7037(96)00008-7)
- Ingri, J., & Pontér, C. (1986). Iron and manganese layering in recent sediments in the Gulf of Bothnia. *Chemical Geology*, *56*(1–2), 105–116. [https://doi.org/10.1016/0009-2541\(86\)90114-2](https://doi.org/10.1016/0009-2541(86)90114-2)
- Jackson, M. J., & Moskowitz, B. (2021). On the distribution of Verwey transition temperatures in natural magnetites. *Geophysical Journal International*, *224*(2), 1314–1325. <https://doi.org/10.1093/gji/ggaa516>
- Jiang, X. D., Zhao, X., Chou, Y. M., Liu, Q. S., Roberts, A. P., Ren, J. B., et al. (2020). Characterization and quantification of magnetofossils within abyssal manganese nodules from the western Pacific Ocean and implications for nodule formation. *Geochemistry, Geophysics, Geosystems*, *21*(3), e2019GC008811. <https://doi.org/10.1029/2019GC008811>
- Jiang, X. D., Zhao, X., Zhao, X., Chou, Y.-M., Hein, J. R., Sun, X., et al. (2021). A magnetic approach to unravelling the paleoenvironmental significance of nanometer-sized Fe hydroxide in NW Pacific ferromanganese deposits. *Earth and Planetary Science Letters*, *565*, 116945. <https://doi.org/10.1016/j.epsl.2021.116945>
- Jiang, X. D., Zhao, X., Zhao, X. Y., Chou, Y.-M., Roberts, A. P., Hein, J. R., et al. (2022). Abyssal manganese nodule recording of global cooling and Tibetan Plateau uplift impacts on Asian aridification. *Geophysical Research Letters*, *49*(3), e2021GL096624. <https://doi.org/10.1029/2021GL096624>

- Joshima, M., & Usui, A. (1998). Magnetostratigraphy of hydrogenetic manganese crusts from Northwestern Pacific seamounts. *Marine Geology*, *146*(1–4), 53–62. [https://doi.org/10.1016/S0025-3227\(97\)00131-X](https://doi.org/10.1016/S0025-3227(97)00131-X)
- Kaikkonen, L., Virtanen, E. A., Kostamo, K., Lappalainen, J., & Kotilainen, A. T. (2019). Extensive coverage of marine mineral concretions revealed in shallow shelf sea areas. *Frontiers in Marine Science*, *6*. <https://doi.org/10.3389/fmars.2019.00541>
- Kars, M., Aubourg, C., & Pozzi, J.-P. (2011). Low temperature magnetic behaviour near 35 K in unmetamorphosed claystones: <50 K magnetic behaviour. *Geophysical Journal International*, *186*(3), 1029–1035. <https://doi.org/10.1111/j.1365-246X.2011.05121.x>
- King, J., Banerjee, S. K., Marvin, J., & Özdemir, Ö. (1982). A comparison of different magnetic methods for determining the relative grain size of magnetite in natural materials: Some results from lake sediments. *Earth and Planetary Science Letters*, *59*(2), 404–419. [https://doi.org/10.1016/0012-821X\(82\)90142-X](https://doi.org/10.1016/0012-821X(82)90142-X)
- Klemm, V., Levasseur, S., Frank, M., Hein, J. R., & Halliday, A. N. (2005). Osmium isotope stratigraphy of a marine ferromanganese crust. *Earth and Planetary Science Letters*, *238*(1–2), 42–48. <https://doi.org/10.1016/j.epsl.2005.07.016>
- Kopp, R. E., & Kirschvink, J. L. (2008). The identification and biogeochemical interpretation of fossil magnetotactic bacteria. *Earth-Science Reviews*, *86*(1–4), 42–61. <https://doi.org/10.1016/j.earscirev.2007.08.001>
- Kosterov, A., Frederichs, T., & von Döbeneck, T. (2006). Low-temperature magnetic properties of rhodochrosite (MnCO₃). *Physics of the Earth and Planetary Interiors*, *154*(3–4), 234–242. <https://doi.org/10.1016/j.pepi.2005.09.011>
- Kuliński, K., Rehder, G., Asmala, E., Bartosova, A., Carstensen, J., Gustafsson, B., et al. (2022). Biogeochemical functioning of the Baltic Sea. *Earth System Dynamics*, *13*(1), 633–685. <https://doi.org/10.5194/esd-13-633-2022>
- Lascu, I., & Plank, C. (2013). A new dimension to sediment magnetism: Charting the spatial variability of magnetic properties across lake basins. *Global and Planetary Change*, *110*, 340–349. <https://doi.org/10.1016/j.gloplacha.2013.03.013>
- Lenz, C., Jilbert, T., Conley, D. J., & Slomp, C. P. (2015). Hypoxia-driven variations in iron and manganese shuttling in the Baltic Sea over the past 8 kyr. *Geochemistry, Geophysics, Geosystems*, *16*(10), 3754–3766. <https://doi.org/10.1002/2015GC005960>
- Li, J., Menguy, N., Roberts, A. P., Gu, L., Leroy, E., Bourgon, J., et al. (2020). Bullet-shaped magnetite biomineralization within a magnetotactic deltaproteobacterium: Implications for magnetofossil identification. *Journal of Geophysical Research: Biogeosciences*, *125*(7), e2020JG005680. <https://doi.org/10.1029/2020JG005680>
- Li, J., Wu, W., Liu, Q., & Pan, Y. (2012). Magnetic anisotropy, magnetostatic interactions and identification of magnetofossils. *Geochemistry, Geophysics, Geosystems*, *13*(12). <https://doi.org/10.1029/2012GC004384>
- Liebetrau, V., Eisenhauer, A., Gussone, N., Wörner, G., Hansen, B. T., & Leipe, T. (2002). 226Raexcess/Ba growth rates and U-Th-Ra-Ba systematic of Baltic Mn/Fe crusts. *Geochimica et Cosmochimica Acta*, *66*(1), 73–83. [https://doi.org/10.1016/S0016-7037\(01\)00766-9](https://doi.org/10.1016/S0016-7037(01)00766-9)
- Lin, W., Wang, Y., Li, B., & Pan, Y. (2012). A biogeographic distribution of magnetotactic bacteria influenced by salinity. *ISME Journal*, *6*(2), 475–479. <https://doi.org/10.1038/ismej.2011.112>
- Liu, Q., Yu, Y., Torrent, J., Roberts, A. P., Pan, Y., & Zhu, R. (2006). Characteristic low-temperature magnetic properties of aluminous goethite [α-(Fe, Al)OOH] explained. *Journal of Geophysical Research*, *111*(B12). <https://doi.org/10.1029/2006JB004560>
- Liu, Y., Li, G. R., Guo, F. F., Jiang, W., Li, Y., & Li, L. J. (2010). Large-scale production of magnetosomes by chemostat culture of *Magnetospirillum gryphiswaldense* at high cell density. *Microbial Cell Factories*, *9*(1), 99. <https://doi.org/10.1186/1475-2859-9-99>
- Marcus, M. A., Edwards, K. J., Gueguen, B., Fakra, S. C., Horn, G., Jelinski, N. A., et al. (2015). Iron mineral structure, reactivity, and isotopic composition in a South Pacific Gyre ferromanganese nodule over 4Ma. *Geochimica et Cosmochimica Acta*, *171*, 61–79. <https://doi.org/10.1016/j.gca.2015.08.021>
- Marcus, M. A., Manceau, A., & Kersten, M. (2004). Mn, Fe, Zn and As speciation in a fast-growing ferromanganese marine nodule. *Geochimica et Cosmochimica Acta*, *68*(14), 3125–3136. <https://doi.org/10.1016/j.gca.2004.01.015>
- Maxbauer, D. P., Feinberg, J. M., & Fox, D. L. (2016). MAX UnMix: A web application for unmixing magnetic coercivity distributions. *Computers & Geosciences*, *95*, 140–145. <https://doi.org/10.1016/j.cageo.2016.07.009>
- Namkung, S., & Lee, G. (2021). Rhodochrosite oxidation by dissolved oxygen and the formation of Mn oxide product: The impact of goethite as a foreign solid substrate. *Environmental Science & Technology*, *55*(21), 14436–14444. <https://doi.org/10.1021/acs.est.1c02285>
- Oda, H., Katanoda, W., Usui, A., Murayama, M., & Yamamoto, Y. (2023). Rotation of a ferromanganese nodule in the Penrhyn Basin, South Pacific, tracked by the Earth's magnetic field. *Geochemistry, Geophysics, Geosystems*, *24*(3), e2022GC010789. <https://doi.org/10.1029/2022GC010789>
- Oda, H., Nakasato, Y., & Usui, A. (2018). Characterization of marine ferromanganese crust from the Pacific using residues of selective chemical leaching: Identification of fossil magnetotactic bacteria with FE-SEM and rock magnetic methods. *Earth Planets and Space*, *70*(1), 165. <https://doi.org/10.1186/s40623-018-0924-3>
- Oda, H., Usui, A., Miyagi, I., Joshima, M., Weiss, B., Shantz, C., et al. (2011). Ultrafine-scale magnetostratigraphy of marine ferromanganese crust. *Geology*, *39*(3), 227–230. <https://doi.org/10.1130/g31610.1>
- Ohenhen, L. O., Feinberg, J. M., Slater, L. D., Ntargiannis, D., Cozzarelli, I. M., Rios-Sanchez, M., et al. (2022). Microbially induced anaerobic oxidation of magnetite to maghemite in a hydrocarbon-contaminated aquifer. *Journal of Geophysical Research: Biogeosciences*, *127*(4), e2021JG006560. <https://doi.org/10.1029/2021JG006560>
- Oldfield, F. (2013). Mud and magnetism: Records of late Pleistocene and Holocene environmental change recorded by magnetic measurements. *Journal of Paleolimnology*, *49*(3), 465–480. <https://doi.org/10.1007/s10933-012-9648-8>
- Özdemir, Ö., & Dunlop, D. J. (2010). Hallmarks of maghemitization in low-temperature remanence cycling of partially oxidized magnetite nanoparticles. *Journal of Geophysical Research*, *115*(B2). <https://doi.org/10.1029/2009JB006756>
- Pike, C. R., Roberts, A. P., & Verosub, K. L. (1999). Characterizing interactions in fine magnetic particle systems using first order reversal curves. *Journal of Applied Physics*, *85*(9), 6660–6667. <https://doi.org/10.1063/1.370176>
- Pike, C. R., Roberts, A. P., & Verosub, K. L. (2001). First-order reversal curve diagrams and thermal relaxation effects in magnetic particles. *Geophysical Journal International*, *145*(3), 721–730. <https://doi.org/10.1046/j.0956-540x.2001.01419.x>
- Pósfai, M., Lefèvre, C. T., Trubitsyn, D., Bazylinski, D. A., & Frankel, R. B. (2013). Phylogenetic significance of composition and crystal morphology of magnetosome minerals. *Frontiers in Microbiology*, *4*, 344. <https://doi.org/10.3389/fmicb.2013.00344>
- Ren, Y., Guan, Y., Sun, X., Xu, L., Xiao, Z., Deng, Y., & He, W. (2023). Nano-mineralogy and growth environment of Fe-Mn polymetallic crusts and nodules from the South China Sea. *Frontiers in Marine Science*, *10*. <https://doi.org/10.3389/fmars.2023.1141926>
- Roberts, A. P. (2015). Magnetic mineral diagenesis. *Earth-Science Reviews*, *151*, 1–47. <https://doi.org/10.1016/j.earscirev.2015.09.010>
- Roberts, A. P., Almeida, T. P., Church, N. S., Harrison, R. J., Heslop, D., Li, Y., et al. (2017). Resolving the origin of pseudo-single domain magnetic behavior. *Journal of Geophysical Research: Solid Earth*, *122*(12), 9534–9558. <https://doi.org/10.1002/2017JB014860>
- Roberts, A. P., Florindo, F., Villa, G., Chang, L., Jovane, L., Bohaty, S. M., et al. (2011). Magnetotactic bacterial abundance in pelagic marine environments is limited by organic carbon flux and availability of dissolved iron. *Earth and Planetary Science Letters*, *310*(3–4), 441–452. <https://doi.org/10.1016/j.epsl.2011.08.011>

- Roberts, A. P., Hu, P., Harrison, R. J., Heslop, D., Muxworthy, A. R., Oda, H., et al. (2019). Domain state diagnosis in rock magnetism: Evaluation of potential alternatives to the day diagram. *Journal of Geophysical Research: Solid Earth*, *124*(6), 5286–5314. <https://doi.org/10.1029/2018JB017049>
- Roberts, A. P., Pike, C. R., & Verosub, K. L. (2000). First-order reversal curve diagrams: A new tool for characterizing the magnetic properties of natural samples. *Journal of Geophysical Research*, *105*(B12), 28461–28475. <https://doi.org/10.1029/2000JB900326>
- Rochette, P., & Fillion, G. (1989). Field and temperature behavior of remanence in synthetic goethite: Paleomagnetic implications. *Geophysical Research Letters*, *16*(8), 851–854. <https://doi.org/10.1029/GL016i008p00851>
- Rodelli, D., Jovane, L., Giorgioni, M., Rego, E. S., Cornaggia, F., Benites, M., et al. (2019). Diagenetic fate of biogenic soft and hard magnetite in chemically stratified sedimentary environments of Mamangá Ría, Brazil. *Journal of Geophysical Research: Solid Earth*, *124*(3), 2313–2330. <https://doi.org/10.1029/2018JB016576>
- Rodelli, D., Jovane, L., Roberts, A. P., Cypriano, J., Abreu, F., & Lins, U. (2018). Fingerprints of partial oxidation of biogenic magnetite from cultivated and natural marine magnetotactic bacteria using synchrotron radiation. *Environmental Microbiology Reports*, *10*(3), 337–343. <https://doi.org/10.1111/1758-2229.12644>
- Shulga, N., Abramov, S., Klyukina, A., Ryazantsev, K., & Gavrilov, S. (2022). Fast-growing Arctic Fe–Mn deposits from the Kara Sea as the refuges for cosmopolitan marine microorganisms. *Scientific Reports*, *12*(1), 21967. <https://doi.org/10.1038/s41598-022-23449-6>
- Stine, J., Geissman, J. W., Sweet, D. E., & Baird, H. (2021). The effect of differential weathering on the magnetic properties of paleosols: A case study of magnetic enhancement vs. magnetic depletion in the Pleistocene blackwater draw formation, Texas. *Frontiers in Earth Science*, *9*. <https://doi.org/10.3389/feart.2021.601401>
- Thierry, S., Dick, S., George, S., Benoit, L., & Cyrille, P. (2019). EMODnet Bathymetry a compilation of bathymetric data in the European waters. In *OCEANS 2019—Marseille. Presented at the OCEANS 2019—Marseille* (pp. 1–7). <https://doi.org/10.1109/OCEANSE.2019.8867250>
- Usui, Y., Yamazaki, T., & Saitoh, M. (2017). Changing abundance of magnetofossil morphologies in pelagic red clay around Minamitorishima, Western North Pacific. *Geochemistry, Geophysics, Geosystems*, *18*(12), 4558–4572. <https://doi.org/10.1002/2017GC007127>
- Vereshchagin, O. S., Perova, E. N., Brusnitsyn, A. I., Ershova, V. B., Khudoley, A. K., Shilovskikh, V. V., & Molchanova, E. V. (2019). Ferromanganese nodules from the Kara Sea: Mineralogy, geochemistry and genesis. *Ore Geology Reviews*, *106*, 192–204. <https://doi.org/10.1016/j.oregeorev.2019.01.023>
- Virtasalo, J. J., & Kotilainen, A. T. (2008). Phosphorus forms and reactive iron in lateglacial, postglacial and brackish-water sediments of the Archipelago Sea, northern Baltic Sea. *Marine Geology*, *252*(1–2), 1–12. <https://doi.org/10.1016/j.margeo.2008.03.008>
- Wagner, C. L., Lascu, I., Lippert, P. C., Egli, R., Livi, K. J. T., & Sears, H. B. (2021). Diversification of iron-biomineralizing organisms during the Paleocene-Eocene Thermal Maximum: Evidence from quantitative unmixing of magnetic signatures of conventional and giant magnetofossils. *Paleoceanography and Paleoclimatology*, *36*(5), e2021PA004225. <https://doi.org/10.1029/2021PA004225>
- Wasiljeff, J., & Kuva, J. (2022). FERMAID preview (version 1) [Dataset]. *Geological Survey of Finland. Fairdata*. <https://doi.org/10.23729/c9377f8c-9978-48d2-8dec-1f0daf2b0eb0>
- Wasiljeff, J., Salminen, J. M., Roberts, A. P., Hu, P., Brown, M., Kuva, J., et al. (2024). Morphology-dependent magnetic properties in shallow-water ferromanganese concretions [Dataset]. *Magnetics Information Consortium (MagIC)*. <https://doi.org/10.7288/V4/MAGIC/20097>
- Winterhalter, B. (1980). Ferromanganese concretions in the Gulf of Bothnia. In I. M. Varentsov & G. Grasely (Eds.), *Geology and geochemistry of manganese III* (pp. 227–254). Hungarian Academy of Sciences.
- Winterhalter, B., & Siivola, J. (1967). An electron microprobe study of the distribution of iron, manganese, and phosphorus in concretions from the Gulf of Bothnia, northern Baltic Sea. *Bulletin de la Commission Geologique de Finlande*, *229*, 161–172.
- Yamazaki, T., Fu, W., Shimono, T., & Usui, Y. (2020). Unmixing biogenic and terrigenous magnetic mineral components in red clay of the Pacific Ocean using principal component analyses of first-order reversal curve diagrams and paleoenvironmental implications. *Earth Planets and Space*, *72*(1), 120. <https://doi.org/10.1186/s40623-020-01248-5>
- Yamazaki, T., & Kawahata, H. (1998). Organic carbon flux controls the morphology of magnetofossils in marine sediments. *Geology*, *26*(12), 1064–1066. [https://doi.org/10.1130/0091-7613\(1998\)026<1064:ocfctm>2.3.co;2](https://doi.org/10.1130/0091-7613(1998)026<1064:ocfctm>2.3.co;2)
- Yli-Hemminki, P., Jørgensen, K. S., & Lehtoranta, J. (2014). Iron–manganese concretions sustaining microbial life in the Baltic Sea: The structure of the bacterial community and enrichments in metal-oxidizing conditions. *Geomicrobiology Journal*, *31*(4), 263–275. <https://doi.org/10.1080/01490451.2013.819050>
- Yu, H., & Leadbetter, J. R. (2020). Bacterial chemolithoautotrophy via manganese oxidation. *Nature*, *583*(7816), 453–458. <https://doi.org/10.1038/s41586-020-2468-5>
- Yuan, W., Zhou, H., Yang, Z., Hein, J. R., & Yang, Q. (2020). Magnetite magnetofossils record biogeochemical remanent magnetization in hydrogenetic ferromanganese crusts. *Geology*, *48*(3), 298–302. <https://doi.org/10.1130/G46881.1>
- Zhamoida, V., Grigoriev, A., Gruzlov, K., & Ryabchuk, D. (2007). The influence of ferromanganese concretions-forming processes in the Eastern Gulf of Finland on the marine environment. *Special Paper - Geological Survey of Finland*, *45*, 21–32.
- Zhamoida, V., Grigoriev, A., Ryabchuk, D., Evdokimenko, A., Kotilainen, A. T., Vallius, H., & Kaskela, A. M. (2017). Ferromanganese concretions of the eastern Gulf of Finland—Environmental role and effects of submarine mining. *Journal of Marine Systems*, *172*, 178–187. <https://doi.org/10.1016/j.jmarsys.2017.03.009>
- Zhamoida, V. A., Butylin, W. P., Glasby, G. P., & Popova, I. A. (1996). The nature of ferromanganese concretions from the eastern Gulf of Finland, Baltic Sea. *Marine Georesources & Geotechnology*, *14*(2), 161–176. <https://doi.org/10.1080/10641199609388309>
- Zhang, F. S., Lin, C. Y., Bian, L. Z., Glasby, G. P., & Zhamoida, V. (2002). Possible evidence for the biogenic formation of spheroidal ferromanganese concretions from the eastern Gulf of Finland, the Baltic Sea. *Baltica*, *15*, 23–29.
- Zhang, Q., Roberts, A. P., Ge, S., Liu, Y., Liu, J., Liu, S., et al. (2022). Interpretation of anhysteretic remanent magnetization carriers in magnetofossil-rich marine sediments. *Journal of Geophysical Research: Solid Earth*, *127*(11), e2022JB024432. <https://doi.org/10.1029/2022JB024432>
- Zhao, X., Heslop, D., & Roberts, A. P. (2015). A protocol for variable-resolution first-order reversal curve measurements. *Geochemistry, Geophysics, Geosystems*, *16*(5), 1364–1377. <https://doi.org/10.1002/2014GC005680>
- Zhao, X., Roberts, A. P., Heslop, D., Paterson, G. A., Li, Y., & Li, J. (2017). Magnetic domain state diagnosis using hysteresis reversal curves. *Journal of Geophysical Research: Solid Earth*, *122*(7), 4767–4789. <https://doi.org/10.1002/2016JB013683>
- Zhong, Y., Chen, Z., González, F. J., Hein, J. R., Zheng, X., Li, G., et al. (2017). Composition and genesis of ferromanganese deposits from the northern South China Sea. *Journal of Asian Earth Sciences*, *138*, 110–128. <https://doi.org/10.1016/j.jseaes.2017.02.015>